Development Of Rapid High-Resolution MR Spectroscopic imaging in the human brain

A thesis submitted to McGill University
in partial fulfillment of the requirements of the degree of
Master of Science

By

Sneha Vaishali Senthil
Integrated Program in Neuroscience
McGill University, Montreal

August 2022

Supervised by Jamie Near

Abstract

Proton Magnetic Resonance Spectroscopy (^{1}H MRS) is a specialised non-invasive modality for identifying and quantifying tissue metabolite concentrations in-vivo. This technique has enabled the detection and assessment of metabolic alterations underlying numerous diseases, ranging from stroke, epilepsy and tumor to neurodegeneration. MRS offers the advantage of studying the biochemical basis of diseases without the infusion of radiolabelled tracers or exposure to ionizing radiation, in contrast to techniques like positron emission tomography (PET) and computed tomography (CT) that limit the number of times a patient can undergo these examinations.

Depending on the required spatial coverage and specific purpose, single-voxel or multivoxel MRS approaches can be employed. While single voxel spectroscopy can be used when the precise volume of interest is defined a priori, multi-voxel spectroscopy, also known as magnetic resonance spectroscopic imaging (MRSI), is highly useful in studying the pathology where the changes occurring in the brain are diffuse or following a characteristic spatial/anatomical pattern. Although MRSI offers numerous potential applications, it is sparingly used as a diagnostic tool because most conventional-MRSI approaches are hampered by prohibitively long scan times, inadequate spatial resolution, low sensitivity, and artifacts. Rapid-MRSI techniques utilizing spatial-spectral encoding have been proposed to address these drawbacks, however, the non-standard pulse sequences needed for rapid-MRSI data acquisitions are not currently provided by clinical scanner manufacturers and the clinical applicability of these methods is yet to be demonstrated.

Additionally, owing to magnetic field drift induced heating of gradient coils and passive shim elements, the acquired MRS/MRSI data are affected by frequency and phase offsets that accumulate between each repetition thereby causing spectral distortion and reduced signal-to-noise ratio (SNR).

In single-voxel MRS, several methods have been established to correct for these drifts. However, drift correction in MRSI data is more challenging because multiple repetitions in most commonly used k-space trajectories do not share common points that can be used to estimate and correct for these offsets.

This project involved the development, implementation and optimisation of a new rapid high-resolution 2D FID-MRSI pulse sequence using a rosette k-space trajectory design. This sequence is capable of providing extremely rapid (~ 2 minutes) encoding of a single 2D-slice in the human brain with high spatial resolution (voxel size: 5x5x10 mm^3), thus allowing reliable quantification of various metabolites in the human brain. This was followed by the development of a new retrospective drift correction method based on spectral registration to estimate and correct for frequency and phase offsets in the acquired MRSI datasets. Finally, the performance of the newly developed MRSI technique was demonstrated in phantom and in human brain *in-vivo*, on both, clinical (3T) and ultra-high-field (7T) MR systems.

The Rosette-MRSI pulse sequence was implemented using the Siemens MR IDEA (Integrated Development Environment for MR Applications) platform on both 3T and 7T whole-body MRI systems. This was followed by phantom and in-vivo validation of the developed technique. A frequency and phase drift correction method based on the previously described spectral registration algorithm was developed and applied to the acquired Rosette-MRSI datasets. This resulted in considerable improvement in the alignment of spectra, spectral peak amplitude/SNR (6.67% increase), and narrower linewidths (5.71% decrease). Finally, Rosette-MRSI acquisitions were performed in healthy human brain at both, 3T and 7T. The expected spectroscopic images were reliably generated at both field strengths; however, some spectral artefacts were present. Further sequence refinements are required in order to reduce the appearance of the observed spectral artefacts and yield clinically usable spectroscopic images.

RÉSUMÉ

La spectroscopie par résonance magnétique du proton (^{1}H MRS) est une modalité non invasive spécialisée pour identifier et quantifier les concentrations de métabolites tissulaires in vivo. Cette technique a permis la détection et l'évaluation des altérations métaboliques sous-jacentes à de nombreuses maladies, allant de l'accident vasculaire cérébral, l'épilepsie et la tumeur à la neurodégénérescence. La SRM offre l'avantage d'étudier la base biochimique des maladies sans perfusion de traceurs radiomarqués ni exposition aux rayonnements ionisants, contrairement aux techniques comme la tomographie par émission de positrons (TEP) et la tomodensitométrie (TDM) qui limitent le nombre de fois qu'un patient peut subir ces examens.

En fonction de la couverture spatiale requise et de l'objectif spécifique, des approches MRS à voxel unique ou multivoxel peuvent être utilisées. Alors que la spectroscopie à voxel unique peut être utilisée lorsque le volume précis d'intérêt est défini a priori, la spectroscopie multi-voxel, également connue sous le nom d'imagerie spectroscopique par résonance magnétique (MRSI), est très utile pour étudier la pathologie où les changements cérébraux sont diffus. Bien que le MRSI offre de nombreuses applications potentielles, il est utilisé avec parcimonie comme outil de diagnostic car la plupart des approches conventionnelles du MRSI sont entravées par des temps de balayage excessivement longs, une résolution spatiale inadéquate, une faible sensibilité et des artefacts. Des techniques MRSI rapides utilisant un codage spatial-spectral ont été proposées pour remédier à ces inconvénients, cependant, les séquences d'impulsions non standard nécessaires pour les acquisitions de données MRSI rapides ne sont pas actuellement fournies par les fabricants de scanners cliniques et l'applicabilité clinique de ces méthodes est encore à venir. être démontré.

De plus, en raison du chauffage induit par la dérive du champ magnétique des bobines de gradient et des éléments de calage passifs, les données MRS/MRSI acquises sont affectées par les

décalages de fréquence et de phase qui s'accumulent entre chaque répétition, provoquant ainsi une distorsion spectrale et une réduction du SNR. En SRM monovoxel, plusieurs méthodes ont été établies pour corriger ces dérives. Cependant, la correction de la dérive dans les données MRSI est plus difficile car les répétitions multiples dans les trajectoires de l'espace k les plus couramment utilisées ne partagent pas de points communs qui peuvent être utilisés pour estimer et corriger ces décalages.

Ce projet impliquait le développement, la mise en œuvre et l'optimisation d'une nouvelle séquence d'impulsions FID-MRSI 2D rapide à haute résolution utilisant une conception de trajectoire en rosette dans l'espace k. Cette séquence est capable de fournir un codage extrêmement rapide (~ 2 minutes) d'une seule tranche 2D dans le cerveau humain avec une résolution spatiale élevée (taille de voxel : 5x5x10 mm3), permettant ainsi une quantification fiable de divers métabolites dans le cerveau humain. Cela a été suivi par le développement d'une nouvelle méthode de correction de dérive rétrospective basée sur l'enregistrement spectral pour estimer et corriger les décalages de fréquence et de phase dans les ensembles de données MRSI acquis. Enfin, les performances de la technique MRSI nouvellement développée ont été démontrées dans le cerveau fantôme et humain in vivo, sur les systèmes IRM cliniques (3T) et à champ ultra-élevé (7T). La séquence d'impulsions Rosette-MRSI a été mise en œuvre sur les systèmes d'IRM corps entier 3T et 7T. Cela a été suivi d'une validation fantôme et in vivo de la technique développée. Une méthode de correction de dérive de fréquence et de phase basée sur l'algorithme d'enregistrement spectral décrit précédemment a été développée et appliquée aux ensembles de données acquis. Cela a entraîné une amélioration considérable de l'alignement des spectres, de l'amplitude de crête spectrale/SNR (augmentation de 6,67 %) et des largeurs de raie plus étroites (diminution de 5,71 %). Enfin, les acquisitions Rosette-MRSI ont été réalisées dans le cerveau humain sain à la fois, 3T et 7T. Les images spectroscopiques attendues ont été générées de manière fiable aux deux intensités de champ ; cependant, d'autres raffinements de séquence sont nécessaires pour produire des images spectroscopiques cliniquement utilisables.

Acknowledgements

I want to extend my heartfelt thanks to a number of people who have helped me throughout the course of my degree and towards the completion of my thesis.

Firstly, I would like to express my deep appreciation towards my supervisor, Dr. Jamie Near, for taking a chance on an international student during the onset of COVID-19. I am truly indebted to him for his continued guidance and support. Ever since I joined his lab, he has served as a constant source of inspiration and has truly helped me to discover my passion for brain research. I have learned a great deal about the importance of never giving up and persevering through the tough times that life may throw at us. I would also like to thank my co-supervisor, Dr. Christine Tardif, for being kind enough to take me under her wing at McGill when Dr. Near had to move to Toronto.

I want to extend my gratitude towards the Tardif lab and Near lab members, for their valuable discussions and creating a friendly atmosphere where I always felt welcomed and, Sajjad Feizollah and Marcus Couch, for their guidance whenever I ran into IDEA problems. I also owe my thanks to my program mentor, Dr. Dominique Walker and my committee members, Dr. David Rudko and Dr. Pedro Rosa-Neto for their critical feedback and suggestions along every step of the way.

I also want to thank my friends, both in Canada and abroad, for always being there for the much-needed virtual focus sessions during the pandemic. They have been a safety net for me through thick and thin and I would not have been able to cope with all the difficulties of moving to Canada and completing my degree without their warmth and support.

And to my home away from home, my second family here in Canada, the Warne family. Marie, James, Emma and Oliver have been a strong pillar of support and I'm grateful beyond words

for their immense love, words of encouragement, kindness, and hospitality. A special thanks to Oliver, for always being there to liven my mood, make me laugh, cook for me, help me whenever possible and listen to me when I needed someone to talk to. I am forever thankful to have you by my side.

Lastly, to my loving family back in India, I would not have been able to make it here today were it not for your constant stream of love, support and wisdom. I have never been away from my parents and sister for this long, yet despite the strenuous time difference and distance between us, they have always been so accommodating to my schedule and have always taken the time to talk to me when I needed them most.

Contribution of authors

Dr. Jamie Near[1,2,3] performed some of the Rosette-MRSI development scans (Section 3.1) and redrafted this thesis. Dr. Marcus Couch[1] assisted in performing development scans at the 7T MRI system at the Montreal Neurological Institute (Section 3.3). Non-cartesian image reconstruction algorithms used throughout this thesis were developed by Brenden Kadota[2] and incorporated into the open access FID-A toolkit. All other material included in this thesis including pulse sequence development, Rosette-MRSI data acquisition, data processing, image reconstruction, analysis, figures and manuscript preparation were produced by Sneha Senthil[1,2,3].

[1] Integrated Program in Neuroscience, McGill University, Montreal, QC, Canada
[2] Hurvitz Brain Sciences Program, Sunnybrook Research Institute, Toronto, ON, Canada
[3] Medical Biophysics Department, Sunnybrook Research Institute, Toronto, ON, Canada

List of tables

List of figures

List of Abbreviations

AD	Alzheimer's disease
ADC	Analog to digital convertor
ALS	Amyotrophic Lateral sclerosis
Cho	Choline
Cr	Creatine
CRLB	Cramer Rao Lower Bound
CT	Computed tomography
DSS	Sodium trimethylsilylpropanesulfonate
EPSI	Echo-planar spectroscopic imaging
FID	Free induction decay
FOV	Field of view
GABA	Gamma-Aminobutyric acid
Gln	Glutamine
Glu	Glutamate
GSH	Glutathione
GUI	Graphical User Interface
IDEA	Integrated Development Environment for MR Applications
Lac	Lactate
Mdh	Measurement data header
mI/Ins	Myo-inositol
MP-RAGE	Magnetization Prepared RApid Gradient Echo
MRS	Magnetic Resonance Spectroscopy
MRSI	Magnetic resonance spectroscopic imaging
MS	Multiple Sclerosis

NAA	N-acetyl aspartate
NAWM	Normal-appearing white matter
NMR	Nuclear magnetic resonance
OVS	Outer Volume Suppression
PCr	Phosphocreatine
PD	Parkinson's disease
PET	Positron emission tomography
PRESS	Point Resolved Spectroscopy
ROI	Region of Interest
SAR	Specific absorption rate
SD	Standard deviation
SNR	Signal-to-noise ratio
SPECIAL	Semi-adiabatic spin echo full intensity acquired localised
STEAM	Stimulated Echo Acquisition Mode
SVS	Single voxel spectroscopy
Tau	Taurine
TE	Echo-time
TMS	Tetramethylsilane
TR	Repetition time
VOI	Volume of interest
WET	Water suppression enhanced through T_1 effects

Chapter 1: Introduction and Literature Review

1. Introduction

Magnetic resonance imaging (MRI) is a versatile technique capable of yielding brain-wide structural, anatomical, functional and metabolic information [1]. Magnetic Resonance Spectroscopy (MRS) is a closely related non-invasive imaging technique that can identify and quantify various tissue metabolites to yield chemical information *in-vivo* without the use of ionizing radiation. MRS uses similar physical principles and detection methods similar to MRI, with an additional feature to detect shifts in resonant frequencies of metabolites due to chemical shifts. Important metabolites in the brain including glutamate (Glu), glutamine (Gln), gamma-Aminobutyric acid (GABA), creatine (Cr), phosphocreatine (PCr), lactate (Lac), myo-inositol (Ins), choline (Cho), N-acetyl aspartate (NAA) and taurine (Tau), among others can be detected using this technique [2, 3]. Each metabolite plays a crucial role in maintaining healthy systemic and cellular functioning [4]. In diseases such as stroke, epilepsy, multiple sclerosis, cancer, Alzheimer's disease, Parkinson's disease and Huntington's disease, pathological changes can lead to altered neurochemical concentrations detectable using MRS [5]. Owing to its extensive use in monitoring metabolic processes in health and disease, MRS has been proven to be a powerful complementary tool to MR imaging sequences [6-8]. Proton (^{1}H) MRS is commonly used in research settings concurrent with MRI.

MRI primarily acquires signals from protons present in water and fat thus making use of the largest available signals while, proton MRS typically acquires signals from protons that are attached to less concentrated molecules and allows measurement of relative and absolute metabolite concentrations. Depending on the required spatial coverage and specific purpose, single-voxel spectroscopy (SVS) or magnetic resonance spectroscopic imaging (or MRSI) may be employed. SVS is the most common technique used for *in-vivo* MR spectroscopy to date [9]. It yields a single spectrum that is used to visualize chemical concentrations in a single targeted region of interest. SVS

is preferred when the precise brain region of interest is well-defined *a priori*. However due to its limited coverage, SVS may not be preferred in cases where the pathology is more diffuse [10].

In contrast to SVS, MRSI (also known as Chemical Shift Imaging (CSI)), yields spectra from a grid or matrix of adjacent voxels thus allowing better spatial coverage. MRSI uses the same phase encoding concepts employed in MRI to map the spatial distribution of MR signals. In the most conventional variant of MRSI, a phase encoding gradient applied between the excitation and the acquisition window allows for the acquisition of one k-space point per repetition time (TR), and this is repeated until the k-space is fully sampled. Once the k-space is filled according to the desired field of view (FOV) and spatial resolution, a three- (or four-) dimensional matrix is obtained with dimensions corresponding to k_x, k_y (and sometimes k_z) and time. Fourier transformation of the acquired matrix along each dimension yields a spectrum at each spatial position, corresponding to the tissue metabolite profile at each location. Maps of individual proton MR-detected metabolite concentrations can be generated throughout the brain to investigate the alterations occurring in the metabolic status of the affected region. However, this technique suffers from intrinsically long acquisition times and very low signal intensity of metabolites which limits its potential in clinical applications. To address these disadvantages, different accelerated MRSI acquisition approaches have been proposed in the past years [11-13]. However, the applicability and validation of these accelerated techniques in disease research is yet to be widely demonstrated.

The acquired spectroscopic data are affected by frequency and phase variations caused due to the magnetic field drift of the scanner over the course of experiment. This reduces the spectral quality of the averaged data which can further affect the quantification of metabolites. In single voxel spectroscopy, methods to correct for these drifts are well established (see section 2.2.1). However, correction techniques for MRSI are not widely available yet, and are required for obtaining improved spectral quality and gains in metabolite signal.

The overall aim of my research project is to develop, implement and optimize a rapid, dynamic, and high-resolution Rosette-MRSI sequence for application in human brain *in vivo*. The

Rosette-MRSI trajectory will provide high resolution and wide spatial coverage in a greatly reduced scan time compared with conventional MRSI. Following this, we will implement a new frequency and phase drift correction method for MRSI and validate it using the MRSI data acquired from the developed Rosette trajectory pulse sequence. The acquired Rosette-MRSI data will be compared on both 3T and 7T human scanner systems to maximise performance and usability in both clinical and scientific research settings.

Background

1.1 Overview of MRS

1.1.1 Basics of NMR spectroscopy

Nuclear magnetic resonance (NMR) is a phenomenon observed in atomic nuclei possessing an odd number of protons or alternatively, neutrons. It was discovered and independently demonstrated by Edward Purcell [14] and Felix Bloch [15] in 1952, the importance of which was recognized by a joint Nobel Prize in Physics in 1952. Following initial animal tissue experiments by *Hoult et al.* [16], the use of proton NMR was demonstrated in the rat brain by Ackerman et al. [17] and *Behar et al.*[18] in the early 1980s. thereby marking the birth of *in-vivo* proton MRS of the brain [18]. Examples of NMR viable nuclei include hydrogen (^{1}H), deuterium (^{2}H), carbon-13 (^{13}C) and phosphorous-31 (^{13}P).

The energy, E, of a magnetic moment in a magnetic field (called Zeeman energy) is given by:

$$E = -\boldsymbol{\mu}.\mathbf{B_0} \qquad (1.1.1)$$

NMR nuclei possess a characteristic magnetic moment ($\boldsymbol{\mu}$) that is related to the quantum mechanical spin angular momentum of the nucleus ($\hat{I}$) by the following formula:

$$\boldsymbol{\mu} = \gamma \boldsymbol{I} \qquad (1.1.2)$$

where γ is the gyromagnetic ratio, a proportionality constant specific to the nucleus (for protons, $\gamma = 42.6$ MHz/T). The spin quantum number, *I* can take only integer or half-integer values as defined by the following set of rules [11, 19]:

i. *I=0* for nuclei with even number of both protons, and neutrons (e.g., ^{12}C, ^{16}O, ^{32}S). In this case, the spins are paired against each other, such that the nucleus has no overall spin.

ii. *I=1,2,3….* (Integer values), for nuclei with an odd number of both, protons and neutrons (e.g., ^{2}H, ^{14}N).

iii. $I = \frac{1}{2}, \frac{3}{2}, \frac{5}{2}$..., (half-integer values) for nuclei with odd mass numbers (e.g., ^{1}H ,^{31}P, ^{23}Na, ^{13}C).

In the quantum mechanical description of NMR, a nucleus with spin quantum number *I* will have *2I+1* orientations in the nuclear ground state. The application of an external magnetic field $\overrightarrow{B_0}$ exerts a weak torque on the nuclear magnetic moment which causes the energy levels to be quantized like the angular momentum, that is, they can only possess a discrete set of values. The possible values of angular momentum (along the z-axis, by convention) are given by the equation:

$$I_z = m\hbar \qquad (1.1.3)$$

where $\hbar = \mathrm{h}/2\pi$ (h: Planck's constant), and the discretized values of *m* are given by the sequence:

$$m = -I, -I+1, \ldots . I-1, I \qquad (1.1.4)$$

For the proton that has spin I=1/2, the allowed values of angular momentum will be $\frac{\hbar}{2}$ (spin up) and - $\frac{\hbar}{2}$ (spin down). The energy and discrete magnetic moment values follow from Eq. (1.1.1) and Eq. (1.1.2) respectively. The difference between two energy levels is given by-

$$\Delta\mathrm{E} = E_- - E_+ = \frac{\gamma\hbar}{2}B_0 - \left(-\frac{\gamma\hbar}{2}\right)B_0 = \gamma\hbar B_0 \qquad (1.1.5)$$

Eq (1.1.5) is an alternative form of Larmor's equation. It represents the energy splitting that occurs when particle possessing a quantized spin is placed in a magnetic field (Figure 1-1).

In thermodynamic equilibrium, the initial populations of the energy levels of the states are described by Boltzmann statistics according to which the lower energy level contains slightly more nuclei compared to the higher energy level, at any temperature. The lowest energy levels correspond to orientations closely aligned to the magnetic field, while those of the highest energy states are aligned opposite to magnetic field.

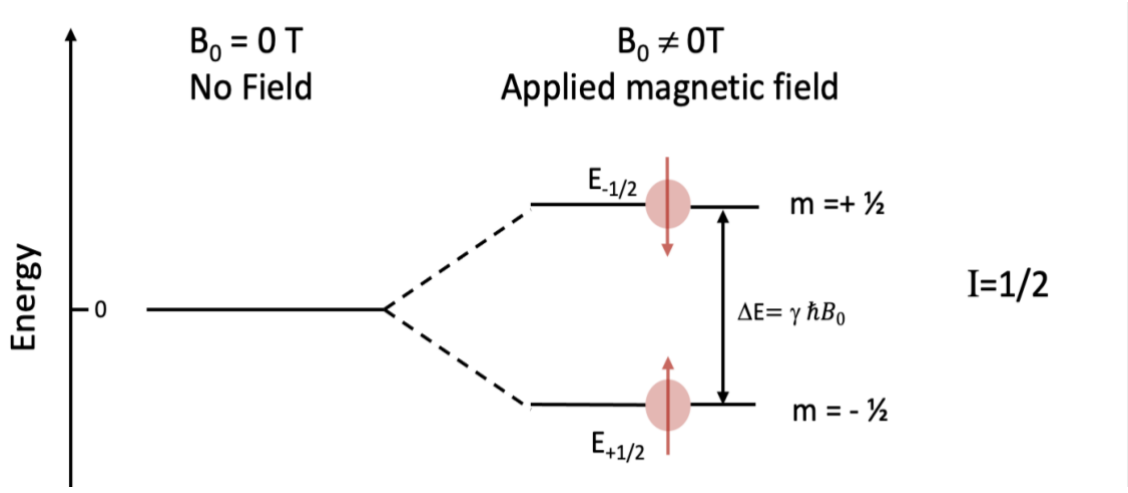

Figure 1-1: Splitting of energy levels in the presence of magnetic field on a single spin ½ nucleus. $E_{+1/2}$ and $E_{-1/2}$ are associated with the aligned and anti-aligned energy states respectively.

The signal in NMR spectroscopy results from the difference between the energy absorbed by spins by jumping from a lower to higher energy state, and the energy emitted by spins that transition simultaneously from the higher to lower energy state. The energy of the photon is quantised in units of $\hbar$ such that, E= $\hbar$ ω where ω is the angular frequency (Planck's quantum theory).

Comparing Eq. (1.1.5) with E= $\hbar$ ω, results in the Larmor condition:

$$\boldsymbol{\omega = \gamma B_0} \qquad \textbf{(1.1.6)}$$

Absorption of a photon that has a frequency equal to the Larmor frequency initiates a transition (or excitation), which is then followed by the emission of a detectable NMR signal, sometimes called a free induction decay, or FID.

1.1.2 Chemical Shift

The structural features of a molecule have an effect on the magnitude of magnetic field experienced and, hence the precessional frequency of the nuclear spin [20]. This underlying concept forms the basis of interpreting an NMR/MRS spectrum. In any given molecule, the electrons surrounding the nucleus exert their own magnetic field, opposed to the main static magnetic field (B_0) thereby producing an 'electronic shielding' effect. This causes the effective magnetic field experienced by the nucleus to be reduced by a factor dependent on the density of surrounding electrons that ultimately causes the resonance frequency, ω_0 for the specific nuclei in the molecule to change.

$$\vec{B}_{local} = \overrightarrow{B_0}\,(1 - \sigma) \qquad (1.1.7)$$

σ is a dimensionless factor known as the shielding constant, usually expressed in ppm (parts per million). In terms of resonant frequency, this leads to:

$$\omega = \omega_0\,(1 - \sigma) \qquad (1.1.8)$$

The resonant frequencies of different chemical species can vary depending on the proton's chemical environment. Eq (1.1.8) implies that the frequency shift also depends on the value of B_0. Thus, a measure of chemical shift independent of the main static field is defined, δ, relative to a reference frequency such that:

$$\delta = \left(\frac{\omega - \omega_{ref}}{\omega_{ref}}\right)10^6 \text{ ppm} \qquad (1.1.9)$$

ω_{ref} is the reference frequency of a standard compound that is ideally maximally shielded such as tetramethylsilane (TMS) or sodium trimethylsilylpropanesulfonate (DSS) (although in practice water is commonly used), and a singlet that is easily recognized in the NMR spectrum. The above-mentioned formula for chemical shift allows us to describe the relative resonance positions in the NMR spectrum. The NMR spectra are conventionally plotted with increasing electronic shielding from left to right that corresponds to a "reversed" frequency axis. A peak at a higher value of chemical shift is *deshielded* in comparison to a chemical shift having a lower value or alternatively, the peak having a lower value of chemical shift is considered to be *shielded* relative to the peak with a higher chemical shift.

1.1.3 Biochemistry of the brain

In MRS, the term 'metabolites' is used as an umbrella term for small molecules which are fundamental to most cellular processes and that contain MR detectable protons. An evaluation of the metabolic composition of the observable metabolites in diseased human tissue can provide information useful to improve diagnosis, staging and monitoring of disease. Metabolites quantifiable with ^{1}H MRS spectroscopy in the brain include glutamate (Glu), glutamine (Gln), myo-inositol (Ins), N-acetylaspartate (NAA), cholines (glycerophosphocholine (GPC) and phosphocholine (PCh)), creatines (creatine (Cr) and phosphocreatine (Cr)), gamma-aminobutyric acid (GABA), lactate (Lac) and taurine (Tau), among others. Figure 1-2 depicts an example of an *in vivo* human brain spectrum acquired by ^{1}H MRS using the semi-adiabatic spin echo full intensity acquired localised (SPECIAL) spectroscopy sequence [21]. The area under a metabolite resonance peak in the MR spectrum is directly related to the concentration of that metabolite.

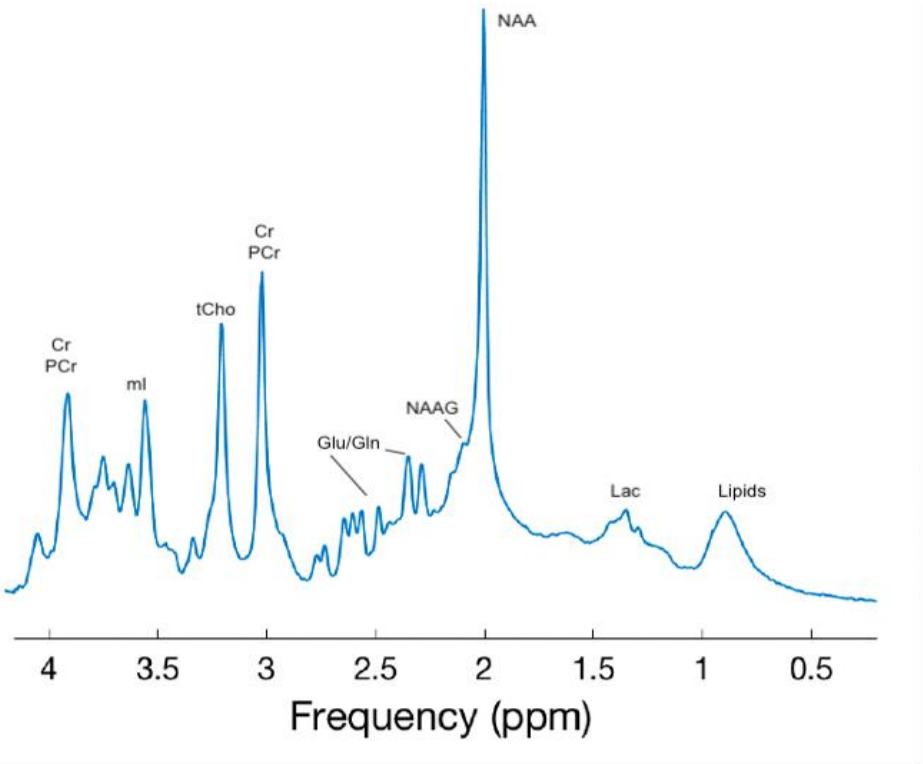

Figure 1-2: Representative ^{1}H MRS spectra acquired from the human brain using the SPECIAL sequence. Selected metabolite peaks are indicated [21].

Glutamate: Glutamate is a non-essential amino acid and the principal excitatory neurotransmitter present in abundance throughout the brain [22]. It plays a crucial role in neuronal signalling, CNS (Central Nervous System) repair and synaptic plasticity involving both glial and neuronal cells [22, 23]. Glu is synthesized in neurons as part of the glutamate-glutamine cycle [24]. Briefly, Glu is synthesized from glutamine in neurons through the action of the enzyme glutaminase in neural tissues and synaptically released during excitatory neurotransmission, and later taken up by astrocytes where it is subsequently converted into glutamine (Gln) by glutamine synthetase (GS). Following this, Gln is released in the extracellular space where it is taken up by neurons and used as a precursor for resynthesizing Glu [25, 26]. ^{1}H MRS can quantify both Glu and Gln with concentrations of Glu being approximately five times higher than Gln. Due to similarity in their structures, Glu and Gln yield similar spectra at 3T however, at higher field strengths, the resulting spectra become

more distinguishable, allowing for individual quantification [27, 28]. The most common resonances for Glu are seen at 3.75 ppm, 2.3 ppm and 2.04 ppm [29].

Glutathione (GSH): Glutathione is an antioxidant responsible for the detoxification of reactive oxygen species in brain cells [30]. The synthesis of GSH involves two enzymatic steps utilizing ATP: first, the formation of γ-glutamylcysteine (from Glu and cysteine) and second, the formation of GSH (from γ-glutamylcysteine and glycine) [31]. GSH is also involved in modulating cell proliferation and apoptosis, transport of amino acids, nutrient metabolism and maintenance of red blood cells. Resonances for GSH are located at 4.6, 3.8, 3.0, 2.5, and 2.1 ppm, though none are distinctly visible in in-vivo brain spectra due to low concentration and overlap with larger peaks [24]. For this reason, J-difference editing techniques are sometimes used to observe GSH.

γ- Aminobutyric Acid (GABA): GABA is a non-protein amino acid that functions as an inhibitory neurotransmitter [32]. GABA exerts its inhibition through two specific receptors classified in terms of their molecular, structural and pharmacological differences as $GABA_A$ and $GABA_B$. GABA is primarily synthesized from the precursor glutamate, in addition to being connected with the metabolism of carbohydrates [33]. GABA is also involved in regulating neuronal activity [32]. GABA spectral lines are centred at 1.89 ppm, 2.28 ppm and 3.01 ppm however, quantification of the metabolite poses a challenge owing its low concentration and large extent of signal overlap with stronger signals from other metabolites [34]. As a result, J-difference editing [35] techniques such as the MEGA-PRESS method [36, 37] are commonly applied for GABA-MRS measurements.

Taurine: Taurine (also known as 2-aminoethanesulfonic acid) is a β-amino acid that serves as an inhibitory neuromodulator in the brain [38]. It is known to modulate cell signaling and

protein phosphorylation [39] and neurotransmitter activity [40, 41]. Taurine also plays a crucial role as an osmoregulator by working as an organic osmolyte [42]. With its ability to prevent cell death and also act as an antioxidant, taurine shows potential for being used in treating neurological disorders like AD, Huntington's disease and stroke [41]. Resonances for taurine are seen at 3.42 ppm and 3.25 ppm.

Myo-inositol (Ins): Myo-inositol is a metabolite present in abundance in the brain mainly present in glial cells thereby serving as a glial marker [43, 44]. Ins is known to mediate osmoregulation, and its phosphorylated derivatives play a crucial role in serving as a second messenger in signal pathways of cells, stimulate protein phosphorylation [45], take part in gene expression, and facilitate export of mRNA from the nucleus [46, 47]. Ins is usually identified by its most prominent peak at 3.56 ppm, although it contains other resonances at 4.05 ppm, and 3.26 ppm.

Cholines (Cho): Choline is a precursor for acetylcholine (ACh), a. neurotransmitter that plays a prominent role in brain and muscle function [48]. It contributes to maintaining the structural integrity and signalling functions of cell membranes [49]. Cho resonance is typically seen at 3.19 ppm however, *in-vivo* ^{1}H MRS yields a broader peak at 3.2 ppm from choline containing compounds- referred to as total choline (tCho). It appears as a single peak incorporating an accumulation of peaks from phosphocholine (3.22 ppm), glycerophosphocholine (3.21 ppm), and free choline (3.19 ppm) [50, 51]. Elevated choline peaks are typically seen in MR spectra of brain tumours [52] and in Alzheimer's disease [53-55].

Creatine (Cr) and Phosphocreatine (PCr): Creatine is a non-protein nitrogenous organic acid that combines with a phosphoryl group to form phosphocreatine that is used in the regeneration of ATP [56]. This makes creatine play an essential role in the network of energy

transfer [57, 58]. *In-vivo* ^{1}H MRS gives a prominent single peak at 3.03 ppm from both, creatine and phosphocreatine [2].

Lactate (Lac): In the brain, lactate is produced when glucose is metabolised via glycolysis [59]. Lactate is present in low concentrations in the brain tissues. Increased Lac concentrations are seen immediately following hypoxia thereby possibly serving as a metabolic marker for cases where blood flow might be disrupted such as, stroke, trauma and tumors [60]. The main resonance of Lac is observed at 1.33 ppm however, owing to its low concentration at rest and the presence of lipid and macromolecule contamination around this spectral region, quantification of Lac poses a difficulty. ^{1}H MRS techniques using long TE times diminish the relative contribution from lipids and can be used to improve Lac quantification [2, 61].

N-acetyl aspartate (NAA): NAA is a free amino acid derivative synthesized in neurons and transported to the cytoplasm of oligodendrocytes [62]. It is the second-most concentrated metabolite in the brain following glutamate. In the context of ^{1}H MRS, NAA presents the largest peak with the most prominent resonance at 2.01 ppm and other resonance peaks ranging from 2.0 ppm to 8 ppm [2]. The levels of NAA quantified using MRS are proposed to serve as markers for neural density, neuronal integrity and metabolism [61-63]. NAA is also believed to have osmoregulatory roles [64] and axon-glial signaling [62]. Alterations in NAA concentrations have been reflected in neurological conditions like MS, Canavan disease [65], schizophrenia and AD [66], and cancer, among others [2, 67].

Macromolecules: The signals from mobile macromolecules (MM) primarily come from protons belonging to amino acids in cytosolic proteins [68, 69]. ^{1}H MRS yields signals from MM when short or intermediate echo times are used. The broad peaks obtained from MM arise from metabolites with narrower peaks and may be potential biomarkers in certain

diseases [70]. MM signals from 0.5-4.5 ppm correspond to protons from methyl, methylene and methine groups and, the MM signals from 5.5-9.0 ppm correspond to aromatic CH and NH protons from amide, amine, and imine groups [70, 71].

1.1.4 Altered neurochemistry and metabolism in brain disease

The neuropathology of various brain diseases is believed to precede the onset of symptoms by years or even decades. MR techniques such as MRI and MRS provide robust, non-invasive assays of brain structure and neurochemistry and have been used to follow the progression of neurological disorders in preclinical and clinical studies [54, 72-74]. The future success of disease modifying treatments will most likely depend on the presence of an ideal and definitive diagnostic tool to identify patients during the presymptomatic stages of the disease. This section reviews the MRS markers of disease progression in common disease conditions like Alzheimer's disease (AD), Parkinson's disease, Multiple Sclerosis, brain tumors and Amyotrophic Lateral sclerosis (ALS).

Alzheimer's Disease:

AD is histopathologically defined by misfolded amyloid-beta (Aβ) peptide deposits and hyperphosphorylation of tau proteins, with other consistent hallmarks being reactive microgliosis, associated astrogliosis, dystrophic neurites (abnormal axons and dendrites) and, neuroinflammation. The downstream consequences of these effects include synaptic and neuronal death, thereby resulting in macroscopic cerebral atrophy [75]. Glucose hypometabolism has been consistently associated with an increased risk of learning and memory deficits concurrent with hyperphosphorylated tau and Aβ deposits. It is known to play a critical and early role in AD pathophysiology by acting as a downstream marker for oxidative stress [76], brain insulin resistance [77], altered thiamine metabolism, and

mitochondrial dysfunction [78]. In recent years, 2-[Fluorine-18] fluoro-2-deoxy-d-glucose ([^{18}F] FDG) positron emission tomography (PET) [79] has been proposed as a suitable imaging modality to visualise glucose metabolism for the early or differential diagnosis of AD [80]. Although FDG-PET offers the possibility to identify patients with suspected AD, its role in identifying patients with MCI that have eventually been diagnosed with AD is less established. Its high heterogeneous sensitivity and specificity can result in the detection of mixed pathologies and may also yield false-positive findings [81, 82]. Even though the radionuclides are not long lasting, exposure to low levels of radiation may limit the number of times one can undergo FDG-PET imaging [83].

Non-invasive imaging modalities like MRS offer an alternative method for tracking the progression of neurodegenerative diseases without exposing subjects to ionizing radiation. Previous studies have reported reduced levels of NAA, glutamate [84] and aspartate and, increased levels of Ins [85], Cho and Glu [86].Furthermore, MRS has been recognized to play a key role in mapping neurochemical concentrations throughout the brain and identifying specific disease patterns of hypometabolism even in the earliest stages of dementia due to AD [87-90].

Parkinson's disease (PD): PD is histopathologically characterized by the degeneration of dopaminergic neurons belonging to the substantia nigra pars compacta (SNc) due to the formation of Lewy bodies and Lewy neurites, primarily composed of intracellular aggregates of α-synuclein [91, 92]. Apart from the SNc, widespread degeneration is also seen in several subcortical nuclei and multiple non-dopaminergic neurons [93]. Cell death in PD is believed to be caused by a multifactorial cascade of events including mitochondrial dysfunction [94], neuroinflammation [95], and disruptive protein clearance processes that remain poorly understood. ^{1}H MRS spectra have shown alterations in metabolic profiles in patients diagnosed with PD [96]. Studies have reported decreased levels of NAA, Glu and glutathione

and elevated Cho levels in SNc compared with control subjects [97, 98]. Investigating the altered neurochemical concentrations using *in vivo* imaging to track underlying pathological mechanisms may provide useful biomarkers for predicting the onset of PD even before symptoms appear.

Amyotrophic lateral sclerosis (ALS): ALS, also commonly known as Lou Gehrig's disease is a fatal, multisystem progressive neuromuscular disorder characterized by the gradual degeneration of cortical and spinal motor neurons giving rise to increased muscle weakness, atrophy and eventually a state of motor paralysis in patients [99]. Death in most patients is attributed to respiratory failure which is frequently caused by pneumonia [100]. Neurochemical changes implying neuronal dysfunction corresponding to reduced NAA detected using MRS are noticeable in the motor cortex and corticospinal tracts. Other metabolic alterations include increases in mI [101], reduced GABA and reduced GSH [102]. Additional MRS studies are needed to map the alterations in metabolic concentrations that would improve the current understanding of the pathophysiology of ALS.

Malignant brain tumors: A brain tumor is an anomalous growth of cells in the brain that multiply uncontrollably, seemingly unfettered by normal cell regulatory processes. Depending on the origin and type of cancer spread, tumors are classified as primary and metastatic. Primary brain tumors originate from brain tissues, or the immediate surrounding tissues of the brain while metastatic tumors arise from cancer cells metastasizing to the brain from a different part of the body. Gliomas are the most common type of primary brain tumors originating in the glial cells of the brain. Results from proton MRS studies have shown remarkably dissimilar spectra in brain tumor patients compared to healthy controls [103]. Elevated Cho levels indicate membrane turnover [104, 105], increase in lactate concentrations is believed to be caused by anaerobic glycolysis [105-108], higher mI levels possibly indicate

the presence of more glial cells [109] and elevated lipid content signaling necrosis and membrane breakdown [105, 110-112].

Multiple Sclerosis (MS): MS is a chronic demyelinating inflammatory autoimmune disease that affects the CNS that leads to severe neurological defects in addition to cognitive and physical disabilities [113]. Four disease courses have been identified for MS: relapsing-remitting MS (RRMS), primary progressive MS (PPMS), secondary progressive MS (SPMS) and progressive relapsing MS (PRMS). MRS serves as a unique tool for assessing the severity of MS, determining a prognosis, understanding pathogenesis, and evaluating the efficiency of therapeutic treatments. Increased levels of mI [114, 115] and decreased levels of NAA and total creatine (tCr) have been reported in the normal-appearing white matter (NAWM) of all subtypes of MS patients. Elevated mI indicates possible glial cell proliferation while lower NAA peaks are a marker of axonal injury and loss [115]. Previous works have shown Glu and GABA also being implicated in disease pathology [116]. Decreased Glu levels in MS mixed tissue [117] and relapsing-remitting mixed tissue [118] and increased Glu levels in NAWM [119] and MS lesions have been observed [119, 120]. Some evidence also suggests increased lactate signals in unspecified [121, 122] and relapsing-remitting MS lesions [123] and, lowered GSH levels in the frontal [124] and parietal cortex [122] .

1.2 Localization techniques in MRS

MR spectra can be obtained by using various nuclei, such as ^{1}H, ^{13}C, ^{19}F, ^{23}Na, and ^{31}P, all of which provide valuable metabolic and physiological information, both quantitatively and non-invasively [125]. Currently, most clinical MR systems are narrow-band systems for proton (^{1}H) imaging, owing to its high abundance in human tissues and relative ease of performance using standard RF coils [126]. For the acquisition of spectra, a region of interest (ROI) is selected where the spectrum is acquired. Depending on the specific

purpose, techniques including single voxel spectroscopy or magnetic resonance spectroscopic imaging (or MRSI) may be employed with either short or long inter-pulse periods (known as echo times or TE).

1.2.1 Single Voxel Spectroscopy

To date, the most commonly used technique for in-vivo MR spectroscopy is single voxel spectroscopy (SVS). SVS yields a single spectrum that is used to visualize chemical concentrations in a targeted volume of interest (VOI). The most basic and widely used ^{1}H MRS techniques at present are STimulated Echo Acquisition Mode (STEAM) [126-128] and Point RESolved Spectroscopy (PRESS) [128, 129]. Both techniques are based on the principle of using three orthogonal gradients that are applied concurrently with three frequency selective pulses in succession. This brings about three slice selections each having an orthogonal orientation, the intersection of which yields the selected volume thereby, localising the voxel of interest. Following this, the resulting echo signal is accrued from the cumulated effect of intersection of the series of three applied RF pulses. To ensure minimum interference with the signal outside the VOI for more signal fidelity, crusher (or spoiler) gradients can be applied carefully during TE on gradient channels to ensure dephasing of the transverse component of magnetization (M_{xy}), thus cancelling unwanted coherences and consequently, any undesired signal. The pulse sequence diagrams of STEAM and PRESS sequences are shown in Figure 1-3. The PRESS sequence comprises of a 90° RF excitation pulse followed by two 180° RF pulses [129]. It yields a greater SNR due to no net magnetization loss during signal localisation however, drawbacks include not being able to achieve shorter echo times (< 30ms) and a greater RF power required for attaining 180° flip angles. STEAM uses three 90° RF pulses for spatial localisation. It has the advantage of being able to achieve very short values of TE (e.g., 7ms) in a single scan [130] and, the use of three 90° RF pulses results in lower RF power demands.

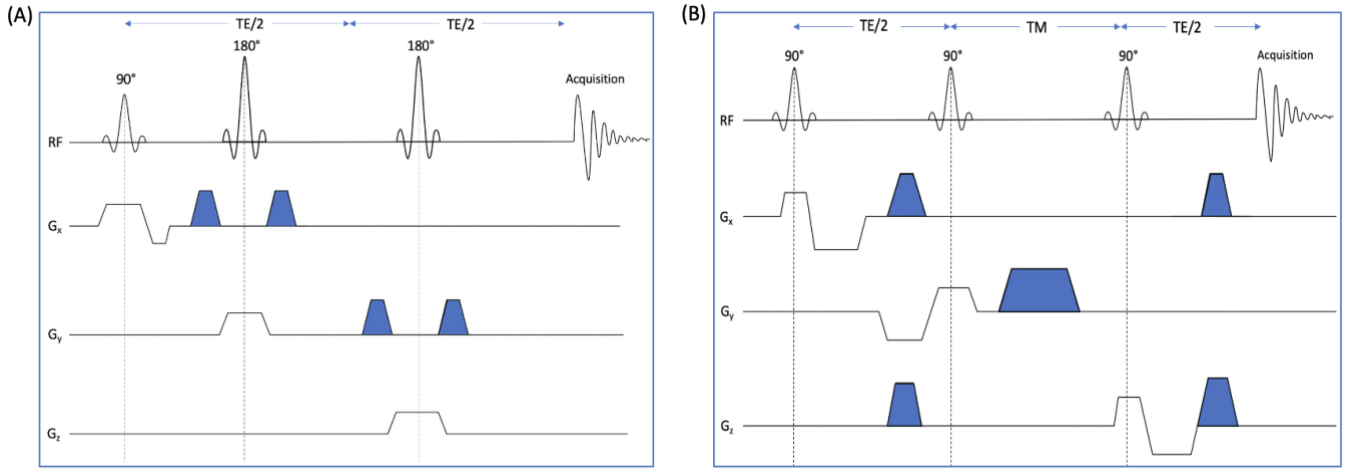

Figure 1-3: Pulse sequence diagrams for (A) PRESS and (B) STEAM sequences. The localization gradients are shown in white, and the spoiler gradients are shaded.

SVS has the advantage of established protocols, being able to achieve good SNR in a comparatively short acquisition time, and good spectral quality with reliable metabolite concentration estimates [131]. SVS is preferred when the precise brain region of interest is well-defined *a priori*. However, due to its limited spatial coverage, SVS may not be preferred in cases where the pathology is more diffuse.

1.2.2 MRSI

In contrast to SVS, Magnetic Resonance Spectroscopic Imaging (MRSI), also known as, Chemical Shift Imaging (CSI), yields spectra from a two or three-dimensional grid of adjacent voxels thus allowing an evaluation of the spatial distribution of metabolite levels within the region being studied [132-134]. MRSI uses the same phase encoding concepts employed in MRI to map the spatial distribution of MR signals.

In the most conventional variant of MRSI, phase encoding is used to acquire one k-space point per repetition time (TR), and this is repeated until k-space is fully sampled (Figure 1-4).

However, in order to achieve high spatial resolution, a large number of phase encoding steps are required which in turn extends the acquisition times significantly [135]. This consequently can lead to patient discomfort and motion artefacts in the acquired spectra. The scan durations for conventional MRSI may limit its routine use in a clinical setting, particularly in the 3D-mode [136]. Due to the long acquisition times required for high-resolution scanning, spatial resolution is often compromised thereby affecting the accurate quantification of metabolites [137]. These underlying limitations have motivated the need for rapid high-spatial resolution MRSI methods.

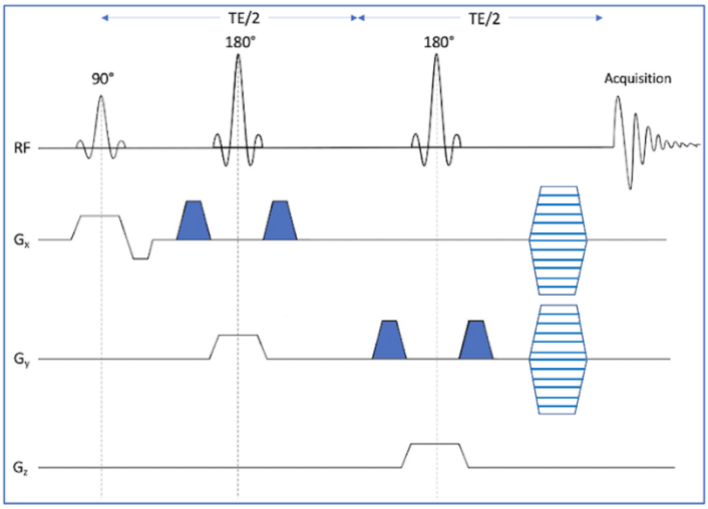

Figure 1-4: Pulse sequence diagram for PRESS-localized MRSI. The added phase encoding gradients can be seen just before the acquisition readout, allowing the recording of a single k-space location per TR.

1.2.3 Rapid-MRSI

MRSI has undergone vast development with regard to spatial coverage, acquisition speed, artefact reduction, spatial resolution, and the quantification of tissue metabolites over more than three decades [1, 13]. To gain higher acceleration in MRSI, spatial-spectral encoding (SSE) was proposed by Peter Mansfield to sample spatial information concurrently with spectral information in contrast to conventional MRSI, where spatial and spectral encoding are strictly discrete [138]. In practice, SSE utilizes a k-space trajectory that repeats over and over to enable temporal sampling (FID acquisition) at each k-space point within a single TR. A variety of different cartesian and non-cartesian sampling schemes utilizing SSE can now be implemented to provide high SNR efficiency and minimal acquisition times. Symmetric Echo-Planar Spectroscopic Imaging (EPSI) and flyback EPSI are the most

commonly used cartesian SSE techniques. Non-cartesian trajectories offer an upper hand over cartesian sampling in terms of their flexibility in sampling k-space, motion insensitivity and the ability to generate images with high spatial-temporal resolution in a reasonable scan time. Examples of non-cartesian SSE techniques include but, are not limited to spiral [139], concentric rings [140], radial EPSI [141], BLADE/PROPELLOR [142], rosette [143] and stochastic trajectories [144].

Rapid high-resolution MRS techniques provide the ability to rapidly map out neurochemical concentrations throughout the brain in neurodegenerative disease research. This will allow observation of the spatial distribution of neurochemical abnormalities in the brain, thus complementing the information provided by FDG-PET and MRI regarding spatial patterns of disease progression.

1.3 Rosette Spectroscopic Imaging

First postulated by Likes [145], the concept of rosette trajectories for spectrally selective MRI was first examined, demonstrated and implemented by Noll and colleagues [143, 146]. Following this, the use of rosette acquisitions for spectroscopic imaging was experimentally investigated by Schirda et al. [147, 148]. A Rosette-MRSI acquisition consists of a non-cartesian, two-dimensional k-space trajectory that is rotating in circular paths in the k_x-k_y plane. To ensure complete sampling of k-space, multiple repetitions are used in a "multishot acquisition" with a different circular path traced during each repetition. One advantage of the 'rosette' trajectory is that the center of k-space is periodically sampled, allowing the possibility for retrospective correction of frequency and phase drift. Furthermore, rosette "rings" never span more than one-half of the full extent of k-space, thus providing an optimal combination of encoding speed, high spatial resolution, and low dwell time (i.e., high spectral resolution, in comparison with some other rapid techniques which must span the full extent of k-space in a single shot (e.g., concentric rings, EPSI, spiral)).

1.3.1 Trajectory design

Each repetition in a rosette acquisition consists of a circular trajectory originating at the center of k-space, with a diameter $k_{max.}$ In each successive repetition, the circles are rotated about the origin during each repetition by an angle of $\varphi = 2\pi n / N_{sh}$ where N_{sh} is the total number of shots and n is the value corresponding to the number of repetitions i.e., n=1,2, 3...N_{sh} until the desired k-space coverage is obtained.

The generalized rosette k-space trajectory can be defined as a complex k-space function given by:

$$\mathbf{k}(t)=k_{max} sin(w_1 t)\, e^{iw_2 t} \tag{1.3.1}$$

where w_1 and w_2 represent the oscillation and rotational frequencies, and the real and imaginary components of k(t) correspond to the x and y components of k (k_x and k_y), respectively. We set $w_1 = w_2$ to achieve circular trajectories. Rosettes offer the relative ease of generating and implementing gradient waveforms and, this is because the gradients vary smoothly in time. The rosette gradients can be obtained by the following equation:

$$\mathbf{G}(t) = \frac{1}{\gamma} \frac{d\,\boldsymbol{k}(t)}{dt}$$

$$= \frac{1}{\gamma} \frac{d\ (k_{max} \sin(wt)\, e^{iwt})}{dt} = \frac{1}{\gamma} k_{max} w\ [\ (cos^2 wt - \sin^2 wt) +$$

$$i(2 \sin(wt) \cos(wt)]$$

$$= \frac{1}{\gamma} k_{max} w(\ cos2wt + isin2wt) \tag{1.3.2}$$

where $G(t)=G_x(t)+ iG_y(t)$ and γ=42.576 MHz/T is the gyromagnetic ratio for protons.

The instantaneous slew rate of the trajectory is given by:

$$\mathbf{S}(t) = \frac{d\boldsymbol{G}}{dt} = \frac{d}{dt}\left(\frac{1}{\gamma} k_{max}\, w\ [cos2wt + isin2wt]\right)$$

$$= \frac{2w^2 k_{max}}{\gamma}\ (-sin2wt + icos2wt) \tag{1.3.3}$$

The magnitude of the slew rate vector is obtained by the square root of its product with its complex conjugate vector:

$$|\mathbf{S}(t)| = \sqrt{\boldsymbol{S}(t).\boldsymbol{S}^{*}(t)} = \frac{2w^2k_{max}}{\text{ɤ}}\sqrt{(-sin2wt + icos2wt)(-sin2wt - icos2wt)}$$

$$|\mathbf{S}(t)| = \frac{2w^2k_{max}}{\text{ɤ}}\sqrt{\sin^2 2wt + \cos^2 2wt} = \frac{2w^2k_{max}}{\text{ɤ}} \qquad (1.3.4)$$

The equations of the above parameters can be visualised in the Figure 1-5 below, that shows the pulse sequence diagram for Rosette-MRSI acquisitions and sampling of rosette trajectories in k-space.

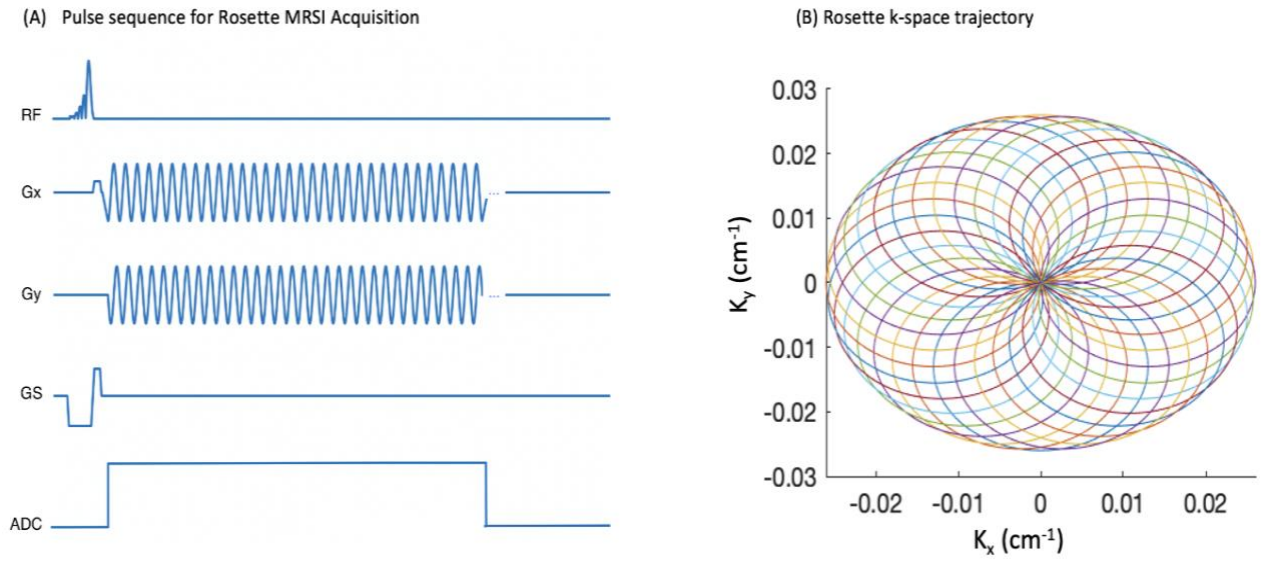

Figure 1-5: (A) Pulse sequence diagram for Rosette-MRSI acquisition showing timing scheme and readout gradients used. (B) Rosette data acquisition trajectories through k-space for a 32-shot pattern. In each TR, one of the circular paths shown is traced repeatedly (512 or more times) to obtain an FID at each point along that path. In subsequent TR's the trajectory is rotated to a different circular path until k-space is fully covered. An important feature of the rosette trajectory is that all circular paths begin at the centre of k-space.

The point spread function (PSF) is a fundamental performance measurement parameter that affects spatial resolution and image quality in MR Imaging and spectroscopic imaging techniques

[149]. The PSF is the Fourier transform of the k-space sampling pattern used in the MRSI acquisition. It gives information about the spatial distribution of signal contributing to a given voxel. The full width at half maxima (FWHM) of the PSF is used to determine the effective spatial resolution. The PSF for a simulated rosette trajectory is shown in Figure 1-6. It shows that the rosette trajectory is highly oversampled in the center and around the edges.

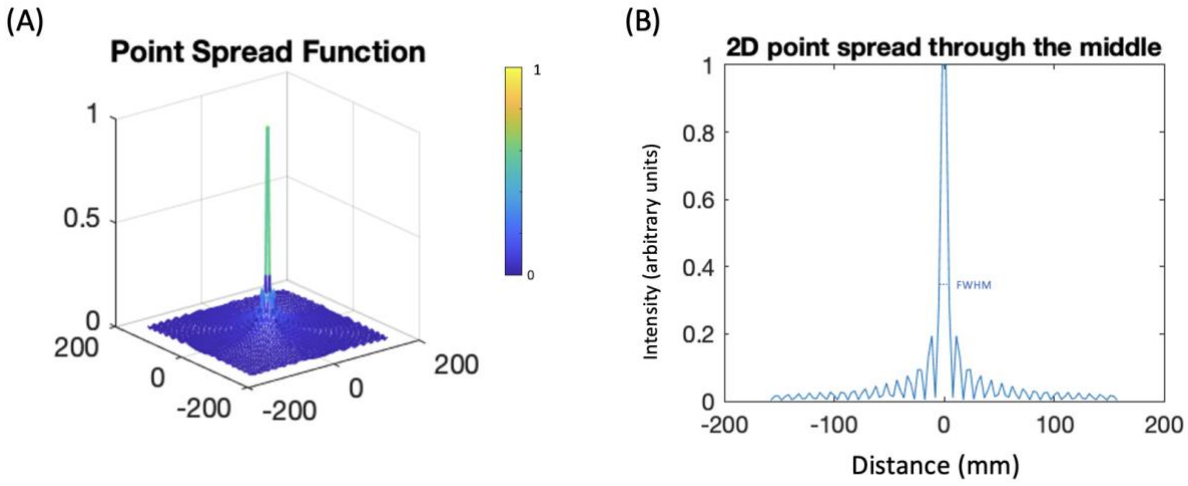

Figure 1-6: (A) Spatial rosette point spread function (PSF) in x-y dimension for simulated rosette dataset with 101 shots and f=4985Hz .(B)Center line profile of 2D PSF for simulated rosette dataset the same parameters and nominal voxel size 5x5x10mm^{3}.

1.3.2 Hardware constraints

Due to physical and instrumental constraints in the MRI system, the magnitude of the trajectory gradient and slew rate are upper-bounded. On a 3T whole-body MRI scanner, the maximum possible limits for gradient amplitude (G_{max}) and slew rate (S_{max}) are 80mT/m and 200 T/m/s respectively. For ultra-high field 7T MRI scanners the typical values of maximum gradient strength and maximum slew rate are also 80mT/m and 200T/m/s respectively. The maximum values of G_{max} and S_{max} cannot be achieved simultaneously due to peripheral nerve stimulation (PNS) constraints.

Gradient constraints- The gradient waveforms represent the velocity of the k-space trajectory at a given time. The peak gradient constraint for rosette trajectories is given by the following equation:

$$|G| \leq \frac{2\pi}{\gamma} k_{max}\omega \quad (1.3.5)$$

Slew rate constraint- The magnitude of peak gradient slew rate is proportional to the acceleration of trajectory and for the rosette trajectory, this is given by:

$$|S| = \frac{2\pi}{\gamma} 2k_{max}\omega^2 \quad (1.3.6)$$

Equations (1.3.5) and (1.3.6) show that both the peak gradient and slew rate increase as a function of spatial resolution (since k_{max}= 1/Δx), and spectral bandwidth ($\Delta\delta$) (since $\omega = \pi\Delta\delta$). In particular, the maximum slew rate increases quadratically with ω thereby causing the maximum achievable spectral bandwidth ($\Delta\delta$) to be primarily constrained by slew rate limitations. These limitations become particularly important at increasing B_0 field strengths since the required spectral bandwidth increases proportionally with B_0. Therefore, to implement rosette trajectories with sufficient spectral bandwidths for MRSI at ultra-high magnetic field strength (i.e., 7T), there is a trade-off between spectral bandwidth and spectral resolution.

Chapter 2: The Current Study

2.1 Rationale

Magnetic resonance spectroscopic imaging is a powerful technique that allows the non-invasive mapping of metabolite concentrations throughout the brain. However, most conventional MRSI approaches are hampered by limited spatial resolution and prohibitively long scan times. The acquired MRS/MRSI data is also characterized by frequency and phase offsets owing to the temporal fluctuations in the B_0 field which are inevitable due to the heating of gradient coils, passive shimming, and subject motion. In single-voxel MRS, drift correction approaches like residual water peak correction [150], Lorentzian lineshape fitting [151] and other non-water suppressed methods such as metabolite cycling [152-155] and spectral registration [156] have been proposed and successfully used. However, correction of frequency and phase drifts in MRSI datasets proves to be more challenging because multiple repetitions often do not share common k-space points that can be used to estimate drifts (e.g., concentric rings, EPSI, conventional MRSI). The overall rationale of this project was to develop, optimise and validate a high-resolution MRSI pulse sequence to quantify metabolites in the human brain. A new frequency and phase drift correction method was developed and applied to the acquired non-cartesian data post-acquisition. Furthermore, the results were compared on both, clinical (3T) and ultra-high field scanner systems (7T) with an aim to maximise performance and usability. The proposed work yielded substantial improvements in acquisition speed and spatial resolution for 2D MRSI acquisition in the human brain. Our long-term goal will be to apply this newly developed sequence towards the study of altered neurochemistry and metabolism in patients with neurodegenerative disorders.

2.2 Aims and hypotheses

Aim 1: To develop, optimise, and validate a rapid high-resolution MRSI pulse sequence based on the rosette k-space trajectory, for mapping metabolite concentrations in the human brain.

Hypothesis: We hypothesized that the newly developed Rosette-MRSI sequence will enable reliable mapping of neurochemical concentrations across an entire 2D slice of the human brain. It will allow MRSI acquisition with a high spatial resolution of ~5 x 5 x 10mm^3, in a scan time of less than 10 minutes.

Aim 2: To develop a new frequency and phase drift correction method to correct for frequency and phase offsets occurring due to heating of gradient coils and passive shimming and apply this correction technique to the acquired Rosette-MRSI data.

Hypothesis: We hypothesized that spectral registration would allow reliable estimation and correction of frequency and phase drifts in rosette spectroscopic imaging data. We further hypothesize that retrospective correction of frequency and phase drifts using spectral registration will result in significant improvements in spectral quality (spectral peak, linewidth, SNR), compared to uncorrected Rosette-MRSI spectra.

Aim 3: To compare the results obtained across clinical and research settings. The Rosette-MRSI sequence will be tested on both clinical (3T) and ultra-high-field (7T) MR systems.

Hypothesis: We hypothesized that Rosette-MRSI will allow whole-slice mapping of neurochemical concentrations in the human brain at both 3T and 7T field strengths. Owing to increased spatial resolution and higher SNR available at higher field strengths, we also hypothesized that 7T Rosette-MRSI will enable the detection of a larger number of metabolites and that quantification precision will be improved at 7T compared to results obtained from the 3T MRI scanner for the same sequence parameters.

Chapter 3: Methodology

3.1 Rapid high-resolution MRSI development

The development of MR sequences for Siemens (3T and 7T) systems requires the use of the Siemens IDEA (Integrated Development Environment for MR Applications) platform that allows for the development of pulse sequences and image reconstruction algorithms for investigational purposes. IDEA also comes with an ICE (Image Calculation Environment) feature for online data processing and image reconstruction. However, the ICE environment was not used, as image reconstruction in this project was performed offline using MATLAB (Mathworks, Natick MA, USA). For Rosette-MRSI sequence development, the desired modifications were made to the FID-CSI product sequence, which is a basic slice-selective pulse-and-acquire MRSI sequence with conventional phase encode gradients. Programming was performed in both the VE11E (for the 3T MRI scanner) and VE12U-SP01 (for the 7T MRI scanner) versions of IDEA.

Prior to the sinusoidal rosette gradients in the in-slice plane, a set of ramp-up gradients was used to smoothly reach the initial rosette gradient amplitudes. To compensate for the area covered by the ramp-up gradients, and to ensure that the rosette trajectories begin at k=0, a set of prephaser gradients were applied prior to the ramp-up gradient, with the same area and opposite polarity to the ramp-up gradients [157]. These prephaser gradients were applied at the same time as the slice refocusing gradient. Care was taken to ensure that the 0^{th} gradient moment along each gradient axis was zero at the beginning of the ADC readout [158]. The accuracy of sequence timing, SAR limits, gradient amplitude limits and slew rate constraints were checked in the sequence simulations. Since the ADC readout supported a limited number of samples per acquisition, multiple ADC event blocks were concatenated to produce a long continuous readout with the ability to acquire more than 80,000 samples per TR. Between each TR, a rotation matrix was used to dynamically update the readout gradients (including phrephaser and ramp-up gradients) in order to sample a different circular path on each TR. Each readout path is associated with a measurement data header (Mdh), which defines

the acquisition number, slice, partition, segment and repetition it belongs to depending on the looping structure of the averaging mode used in the sequence.

Pulse Sequence Parameters

The number of excitations (or shots) used in the rosette trajectory dictates the density of k-space sampling for an individual slice and hence, proper coverage of k-t space. The desired number of pixels in the final image matrix (N_x, N_y, here we assume a square matrix such that $N_x = N_y$) directly relates with the number of excitations (N_{sh}) used and is depicted by the following equation [148]:

$$N_{sh} = \frac{\pi N_x}{2} \tag{3.1}$$

The highest spatial frequencies i.e., the largest coordinates in k-space, denoted by $\pm k_{max}$ are given by [148]:

$$k_{max} = \frac{N_x}{2\,FOV} \tag{3.2}$$

where the FOV is in mm and k_{max} is in mm^{-1}. From equation (2.3.2), we can see that *k* is proportional to the area under the gradients used and duration *t*. The maximum gradient amplitude (G_{amp}) in mT/m is given by [148]:

$$G_{amp} = \frac{1000 k_{max} \omega}{\gamma} \tag{3.3}$$

where γ (for ^1H) = 42.58 MHz/T and ω is the oscillation (or rotational frequency) related to spectral bandwidth ($\Delta\delta$) by the formula $\omega = \pi\Delta\delta$.

During each excitation, the circular trajectory is rotated about the origin with respect to the first trajectory by an angle $\phi = 2\pi\, n/ N_{sh}$ where n= 1, 2…N_{sh}. Each circle is traversed multiple times (≥512 times) in a single repetition in order to achieve temporal / chemical-shift encoding at each k-space position.

The time resolution of the gradient system, also known as the gradient raster time (t_G), has a default value of 10μs in IDEA. According to the Nyquist-Shannon sampling theorem, the k-space sampling rate must be at least twice the highest frequency measured in order to avoid aliasing artefacts and fully reconstruct the data. The analog-to-digital converter (ADC) dwell time (dt_{ADC}) thus, must be smaller or equal to the Nyquist limit [148].

$$dt_{ADC} = \frac{1}{\Delta\delta \left(1 + \frac{\pi N_x}{2}\right)} \tag{3.4}$$

Due to hardware restrictions, the readout gradients and ADC operate with different dwell times. However, they need to satisfy the following condition to ensure that each individual pass of the circular path is sampled with an integer number of gradient and ADC samples:

$$dt_{ADC}. n_{ADC} = n_G. t_G \tag{3.5}$$

where n_{ADC} is the integer number of ADC points and n_G is the integer number of gradient sample points in an individual pass of the circular rosette path. Equation (3.5) implies that the duration of the ADC event should be equal to gradient readout duration.

The developed sequence supported the use of short-term averaging (STA) as well as long-term averaging (LTA) modes. In STA, each shot in k-space is traversed within all averages before moving to the next shot. Conversely, in LTA, all shots are traversed before repeating signal averages.

Data Acquisition

An FID-based, two-dimensional (2D) Rosette-MRSI pulse sequence with the above-mentioned gradient design was tested at the 3T Prisma MR (Siemens, Erlangen, Germany) at Sunnybrook Research Institute (SRI), Toronto, Ontario with a 20-channel phased array head coil and,

the following parameters: $\Delta\delta$ = 1587 Hz, N_{sh}= 101, FOV=320mm, FA (flip angle) =60^0, 64x64 matrix size (N_x = 64), 4 preparation scans, 4 averages, TR/TE=700/1.8ms, nominal voxel size, 5x5x10mm^3, 4032 gradient/ADC sample points per block, 64 loops per block, 8 blocks , 512 loops per TR, 126 ADC points per k-space loop, WET (water suppression enhanced through T_1 effects) suppression with 3 pulses with duration 25.6ms each and 80Hz pulse bandwidth [159] and total scan time ~9min. Prior to the Rosette-MRSI scan, a 3D T_1-weighted, MP-RAGE (Magnetization Prepared RApid Gradient Echo) [160] image was acquired for localisation purposes. The whole-body MAGNETOM Prisma scanner can achieve a maximum gradient performance of 80mT/m and slew rate of 200 T/m/s. Using a spectral bandwidth ($\Delta\delta$) of 1587Hz yielded a rosette angular frequency (ω) of 4986.66 rad/s. The corresponding peak gradient strength was calculated to be 11.71 mT/m along the x- and y-directions and 7.28 mT/m along the z-direction. The peak slew rate in the x- and y- directions was 127.97 T/m/ms and 36.66 T/m/ms along the z-direction.

Phantom MRSI data were acquired using a "Braino" phantom (GE Medical Systems, Milwaukee, WI, USA) that contains realistic relative concentrations of typical human brain metabolites. The averaging mode was set to LTA wherein the signal averages were collected after executing all phase encoding steps for the desired k-space coverage. Data were extracted from the scanner console in TWIX (.dat) format that contains individual raw FIDs for each RF channel and repetition. Online data processing via ICE was disabled and all image reconstruction was performed offline.

Following phantom experiments, a healthy human volunteer (female; age 22) was scanned on the same MR system using the same experimental protocol and imaging parameters in order to capture the additional motion-related frequency and phase variations that are not seen in phantom results.

Data Processing and Reconstruction

Data processing and reconstruction were performed in MATLAB (MathWorks, Natick, Massachusetts) using the FID-A Toolkit [21]. First, k-space density compensation was performed

using the Voronoi density estimation method [161, 162]. Spatial Fourier transform was performed following which coil channels of the MRSI data were combined. To do this, the coil's phases were first adjusted to match the phase of the first coil. Then, sensitivity weights for coils were estimated by the formula $w(i) = S(i)/\sqrt{sum(S^2)}$ where S is the intensity of k=0 FIDs and *i* is the coil number. Coils were then summed by the equation $F = sum(W(i) * f(i))$, where $W(i)$ is the i^{th} coil's sensitivity weight, $f(i)$ is the i^{th} coil FIDs and F is the final summed signal [163]. This way, signals from multiple coil channels was optimally combined resulting in high SNR at every image voxel. The phase and weight maps calculated for the coil combination of water unsuppressed data was applied to the water suppressed data after which, spectral Fourier transform was performed to obtain the resulting 64x64 MRSI grid. Residual water peak removal was implemented using L2 regularization [164]. The *in-vivo* MRSI data was Hamming filtered in an attempt to remove lipid contamination which was further reduced by performing L2 regularization in the lipid resonance range ([0.3-1.9 ppm]) [165]. B_0 correction was performed to correct for slight B_0 shifts across all voxels in the acquired MRSI grid. Using an FID sequence with an echo-delay of 1.8ms introduced a small first order phase error which was corrected for using FID-A.

3.2 Frequency and phase drift correction

FIDs from the centre of k-space were isolated from each repetition by extracting the first and each subsequent 126th point of each ADC readout (126 being the number of ADC points per k-space loop). Using the first k=0 FID as reference, frequency and phase offsets for each subsequent repetition were estimated using time-domain spectral registration, which uses non-linear least-squares minimization to estimate the frequency and phase shift required to optimally align each FID signal to the reference spectrum. Each nth FID $S_n(t)$ is aligned to a reference FID R(t) by adjusting its frequency, f (Hz) and phase, ϕ (degrees) using the following equation:

$$\min_{f,\phi} ||R(t) - G_m(t, f, \phi)||_2 \quad (3.6)$$

where

$$G_m(t, f, \phi) = S_m(t)\exp\left(2\pi\left(ft + \frac{\phi}{360}\right)\right) \quad (3.7)$$

This minimization was implemented in MATLAB (MathWorks, MA, USA) using the 'nlinfit' function provided by the MATLAB Statistics toolbox that returns the least square parameter estimates based on the Gauss-Newton algorithm with Levenberg-Marquardt modifications for global convergence. Once the frequency and phase offsets were estimated for each k=0 FID, the corresponding corrections were applied to the full ADC signals (not only the k=0 extracted FIDs), to achieve a frequency and phase drift correction across the whole of k-space. Estimation and correction of drifts were performed individually for each RF channel. The MATLAB code is provided in the FID-A repository on GitHub [21]. The performance of time-domain spectral registration was assessed by visual inspection of frequency and phase drift curves and the metabolite spectral quality before and after correction. Furthermore, SNR (amplitude of the NAA peak divided by the standard deviation of the noise) of the water unsuppressed data and, NAA linewidths and NAA peak heights from water suppressed datasets were compared before and after drift correction to assess improvements in spectral quality.

3.3 Data acquisition at 7T

Rosette-MRSI was tested at the ultra-high-field 7T Terra whole-body MR scanner (Siemens, Erlangen, Germany) housed at the Montreal Neurological Institute, to investigate possible improvements in SNR and spectral quality resulting from higher B_0 field strength. Prior to the Rosette-MRSI scan, a 3D T_1-weighted, MP-RAGE (Magnetization Prepared RApid Gradient Echo) [160] image was acquired for localisation purposes. Phantom experiments were performed using the GE "Braino" phantom prior to acquiring *in-vivo* data, using a 32-channel receive coil array combined with a volume transmit coil (Nova Medical, Wilmington, MA). The imaging parameters used were as follows: $\Delta\delta$ = 2500 Hz, N_{sh}= 76, FOV=336mm, FA (flip angle) =60^0, 48x48 matrix size (N_x = 48), 4 preparation scans, 4 averages, TR/TE=700/1.8 ms, nominal voxel size 7x7x10mm^3, 5760 gradient/ADC sample points per block, 144 loops per block, 6 blocks, 864 loops per TR, 80 ADC

points per k-space loop, WET water suppression with with 3 pulses with duration 25.6ms each and 80Hz pulse bandwidth [159] and total scan time ~8min. The whole-body MAGNETOM Terra scanner uses gradient coils that can achieve a maximum gradient performance of 80mT/m and slew rate of 200 T/m/s. Using the higher spectral bandwidth ($\Delta\delta$) of 2500Hz yielded an angular frequency (ω) of 7854 rad/s. The corresponding peak gradient strength was calculated to be 13.09 mT/m along the x- and y- direction and 10.55 mT/m along the z-direction. The peak slew rate in the x- and y-direction was 196.97 T/m/ms and 35.17 T/m/ms along the z-direction.

Data processing and reconstruction were performed using the same procedural protocol used for processing Rosette-MRSI data at 3T.

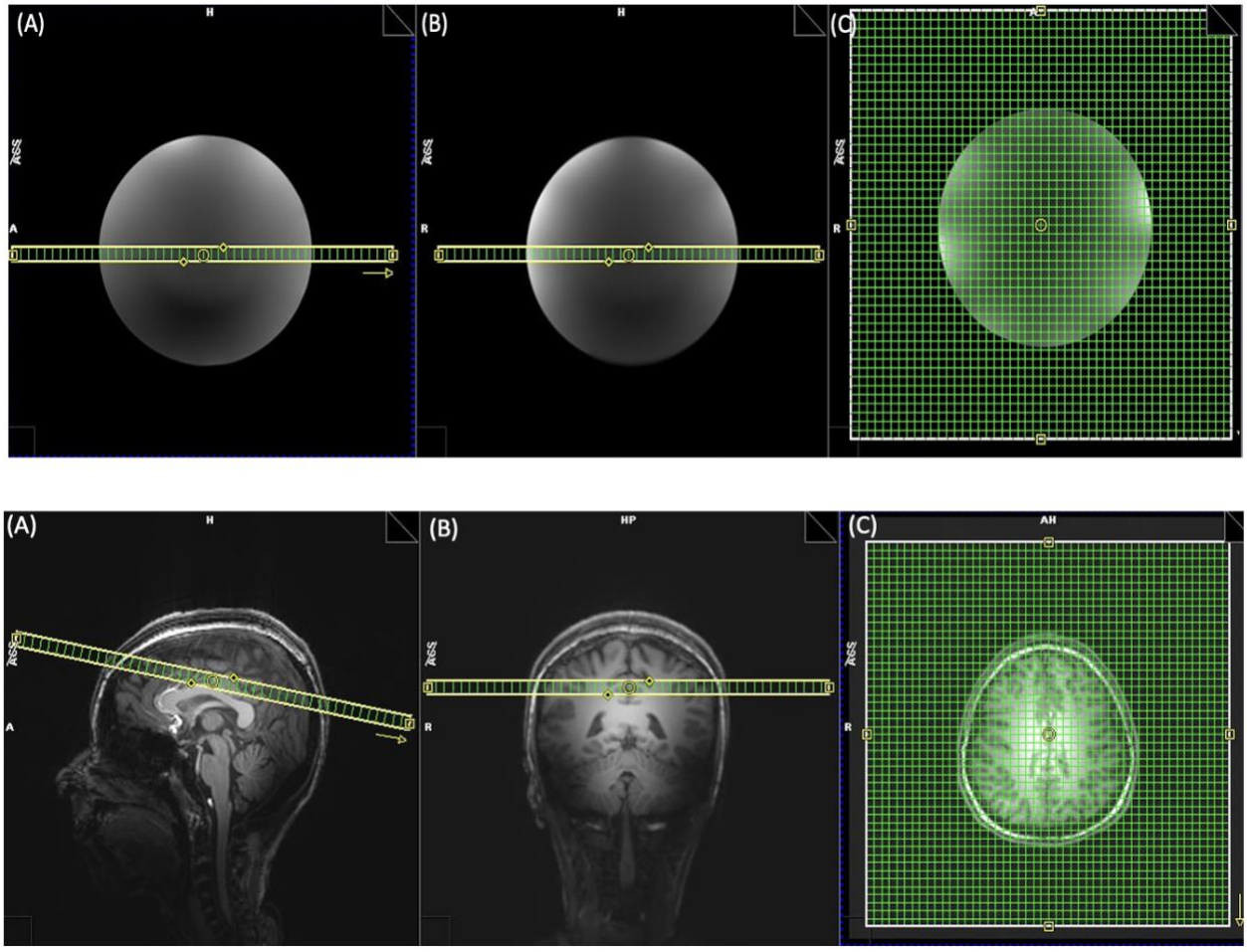

Figure 3-1: (A) Sagittal (B) coronal and (C) axial views of the acquired phantom (upper) and in-vivo (lower) Rosette-MRSI slice (48x48 matrix) positioned on a T_1-weighted image at 7T.

Metabolite quantification

Phantom data were analyzed using LCModel to estimate the concentrations of metabolites. The LCModel basis sets for 3T and 7T included spectra of 14 brain metabolites: alanine (Ala), aspartate (Asp), creatine (Cr), phosphocreatine (PCr), PCh, GABA, Gln, Glu, GSH, mI, Lac, NAA, scyllo-inositol (Scyllo), Asc (ascorbate), GPC, glucose and Tau. The LCModel analysis was performed on spectra within the chemical shift range 0.5 ppm - 4.2 ppm. Cramer-Rao lower bound (CRLB) gives the lower estimate for the variance of an unbiased estimator (LCModel). Data with CRLB >20% and linewidths>20Hz were eliminated from further analysis. CRLB values for 3T and 7T LC model quantified data and the resulting relative concentration estimates and, corresponding standard deviations (SDs) were compared to evaluate the differences in the accuracy of metabolite quantification between both scanners. In total, 7 individual compounds were estimated at 3T, and 12 individual compounds were estimated at 7T as per the above criteria.

Chapter 4: Results

4.1 Rapid high-resolution MRSI development

The Rosette-MRSI pulse sequence was developed on both, VE11E (for 3T) and VE12U-SP01 (for 7T) versions of IDEA. The sinusoidal rosette gradient frequency for the sequence was chosen to avoid the mechanical system resonance frequency range for each scanner. Protocol parameters were modified to investigate the behaviour of the sequence and the graphical user interface (GUI). The handler functions were automatically adapted to all parameters necessary to fix the protocol in cases of parameter conflict. Figure 4-1 shows a simulation of the rosette pulse sequence for the 64-shot Rosette-MRSI trajectory used for the aforementioned validation experiments.

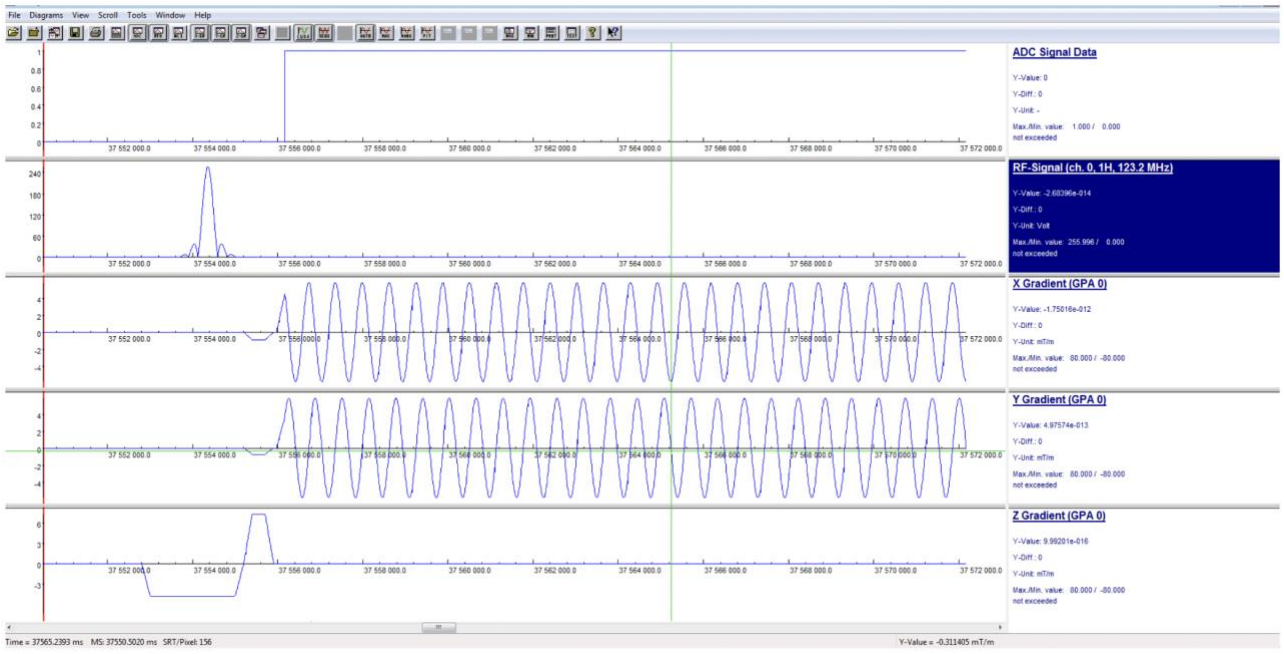

Figure 4-1: Siemens IDEA sequence simulation tool showing the timing and amplitudes of the various pulse sequence elements for the rosette sequence, including RF pulses, ADC events, rosette gradients (along x- and y- directions) and slice select gradient (along z- direction).

Following phantom and *in-vivo* data acquisition at 3T and data processing, the final 64x64 Rosette-MRSI grids were obtained. While the phantom spectroscopic data were reliably generated with very good spectral quality, the in-vivo spectroscopic data were contaminated by some spectral artifacts

around the lipid resonance range and baseline distortions (Figure 4-2). These effects were most prominent near the edge of the brain (close to extracranial lipids), however were observed throughout the brain. Further sequence refinements are required in order to perform prospective lipid suppression which is believed to further minimise the artifacts. Despite the presence of artifacts, the main metabolite resonances of NAA, choline and creatine are clearly visible in the in-vivo MRS data with sufficient SNR, thus supporting the first hypothesis that Rosette-MRSI would enable high-resolution MRSI of the brain in under 10 minutes. Figure 4-3 shows the full MRSI matrices for a phantom scan (A) as well as an *in-vivo* human brain scan following L2 regularization processing to remove lipid contamination (B).

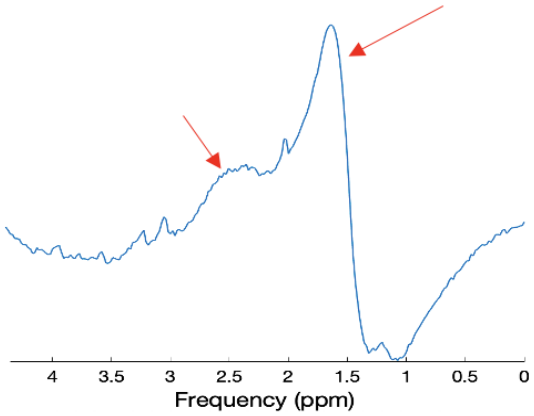

Figure 4-2: ^{1}H spectrum plotted from a voxel obtained from the water suppressed in-vivo data. High lipid contamination (red arrows) is seen in the lipid resonance range [0.5-1.9 ppm].

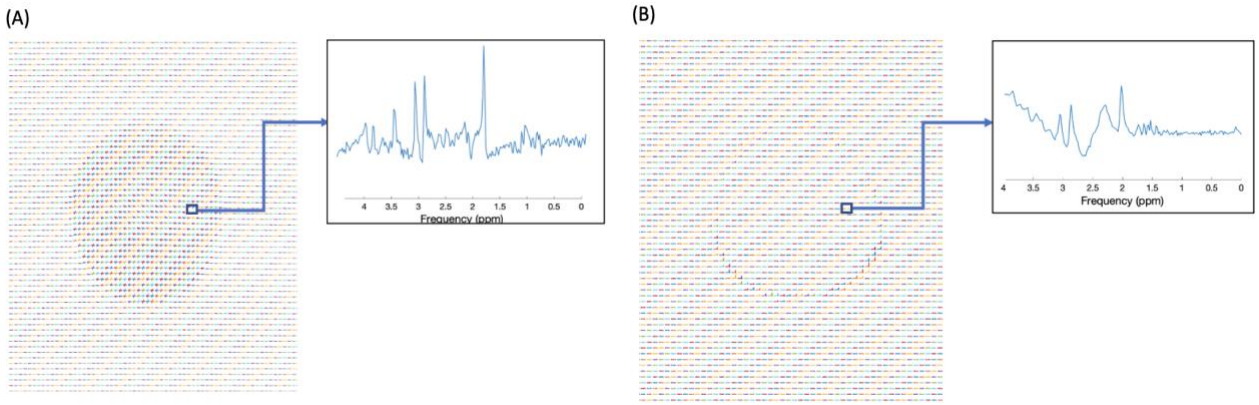

Figure 4-3: MRSI plots of reconstructed and processed water suppressed Rosette-MRSI (A) phantom and (B) in-vivo data at 3T. Prominent lipid contamination in the *in-vivo* dataset was removed in post-processing using L2 regularization.

4.2 Frequency and phase drift correction

Phantom experiments

Results of the Rosette-MRSI acquisition and frequency and phase drift measurement in phantoms are shown in Figure 4-4. The resonant frequency drifted approximately linearly by a total of 3.9Hz and the phase drift ranged from -1.5° to 3° across all scans during the 10-minute acquisition duration. Figure 4-5 demonstrates the alignment of k=0 FIDs to the reference spectrum during spectral registration. Spectral registration resulted in a noticeable improvement in spectral linewidths, SNR and spectral peak heights.

Water suppressed spectra from an arbitrarily selected voxel of interest in the reconstructed MRSI grid are shown in Figure 4-6, both before and after drift correction. Frequency and phase drift correction resulted in a noticeable improvement in SNR, spectral linewidths and the lineshape of metabolite peaks. Figure 4-7 shows NAA SNR, NAA linewidth and NAA peak height maps before and after drift correction. Table 4-1 gives the average values of SNR, NAA linewidth and NAA peak height measured before and after drift correction in the phantom spectra. The average values of SNR increased by ~6.5% [$t(1244)=5.50$, $p<0.001$], NAA linewidth improved by ~7.8% [$t(1942)=5.37$, $p<0.001$] and NAA peak height increased by ~6% [$t(1798)= -16.10$, $p<0.001$].

Table 4-1

Mean values of SNR, NAA linewidth and NAA peak measured for phantom spectra before and after drift correction using spectral registration at 3T.

	Mean SNR ± SD	Mean NAA linewidth ± SD (Hz)	Mean NAA peak height ± SD (arbitrary units)
Before spectral registration	145.38± 30.50	3.83±0.63	0.35± 0.12

After spectral registration	155.09± 25.54	3.53± 1.62	0.37± 0.16

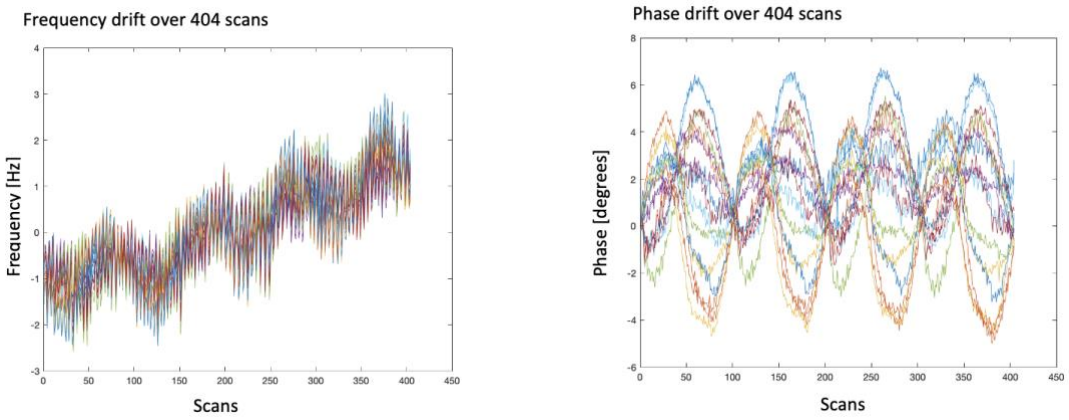

Figure 4-4: (A) Plot of frequency drift measured for each coil channel and shot over 404 scans (101 shots x 4 averages). The total drift was estimated to be 0.39Hz/min in the phantom, with a total drift of 3.9Hz. (B) The phase drift measured for each coil channel and shot over 404 scans. The estimated phase drift did not exceed ±5 degrees.

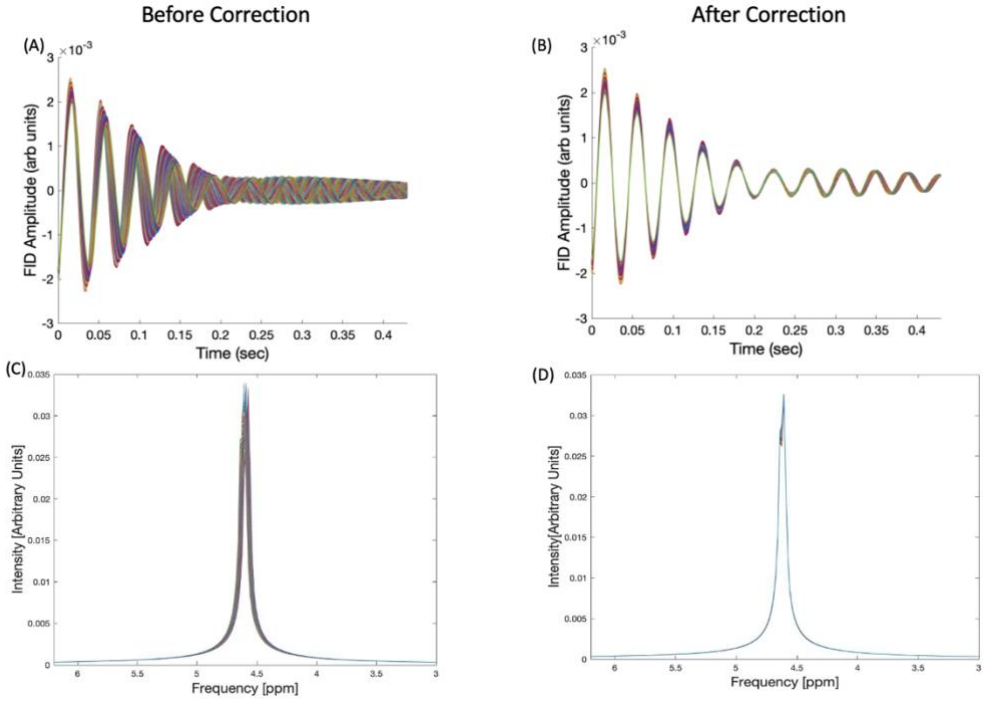

Figure 4-5: Demonstration of FIDs from the center of k-space are plotted for all scans ((A) and (B)) with their corresponding spectra ((C) and (D)) before (left) and after (right) frequency correction using time-domain spectral registration. The alignment of both, FIDs and spectra are visually improved following spectral registration.

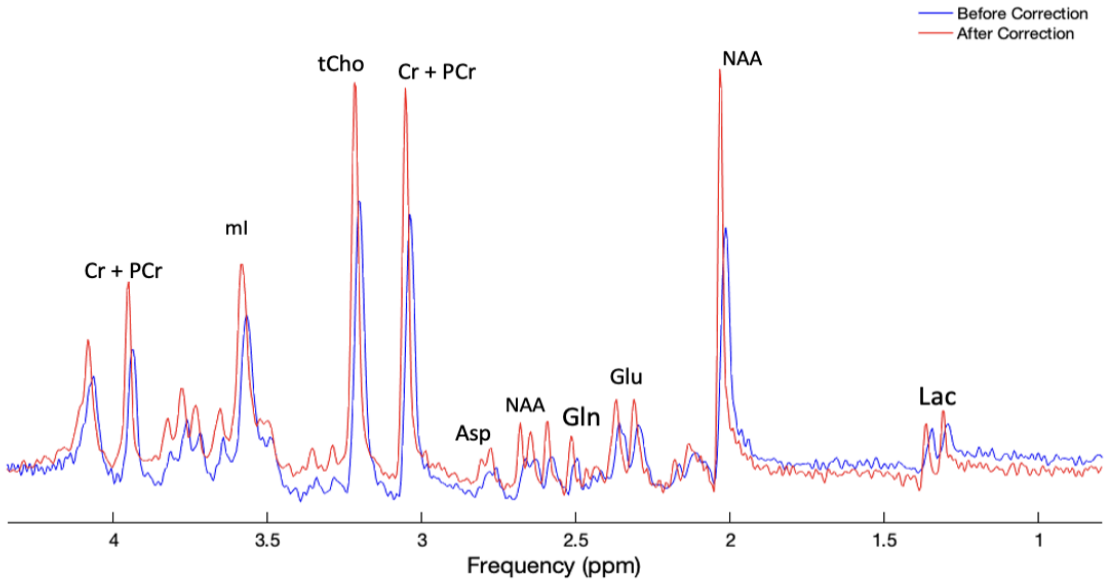

Figure 4-6: Corrected (red) and uncorrected (blue) MRS spectra from one voxel of the Rosette-MRSI acquisition in a phantom with N_x=64, after processing. The spectral quality (linewidth, peak heights and SNR) is noticeably improved following the implementation of spectral registration.

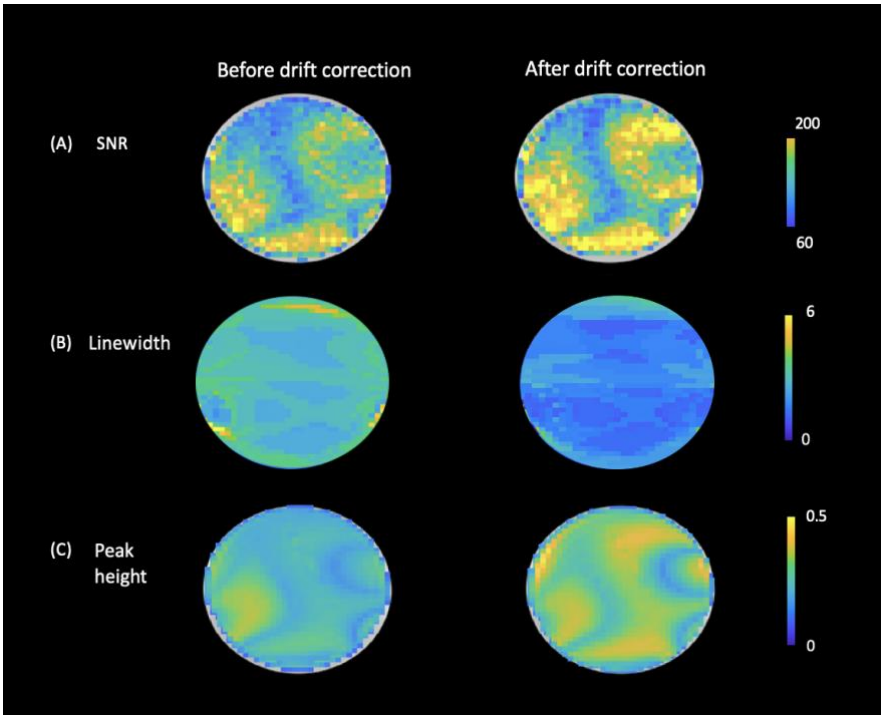

Figure 4-7: (A)SNR (measured as the amplitude of the NAA peak divided by the standard deviation of the noise), (B)NAA Linewidth and (C) NAA peak height maps in 64x64 resolution showing pixel intensity distribution across the whole 2D-phantom slice, before and after drift correction. Spectral registration yielded higher SNR, narrower linewidths and improved peak heights across the MRSI grid.

In-vivo experiments

Results of the Rosette-MRSI acquisition and frequency and phase drift measurement *in-vivo* are shown in Figure 4-8. The resonant frequency drifted approximately linearly by a total of 3.6Hz and the phase drift ranged from -3.8° to 0.5° across all scans during the 10-minute acquisition duration.

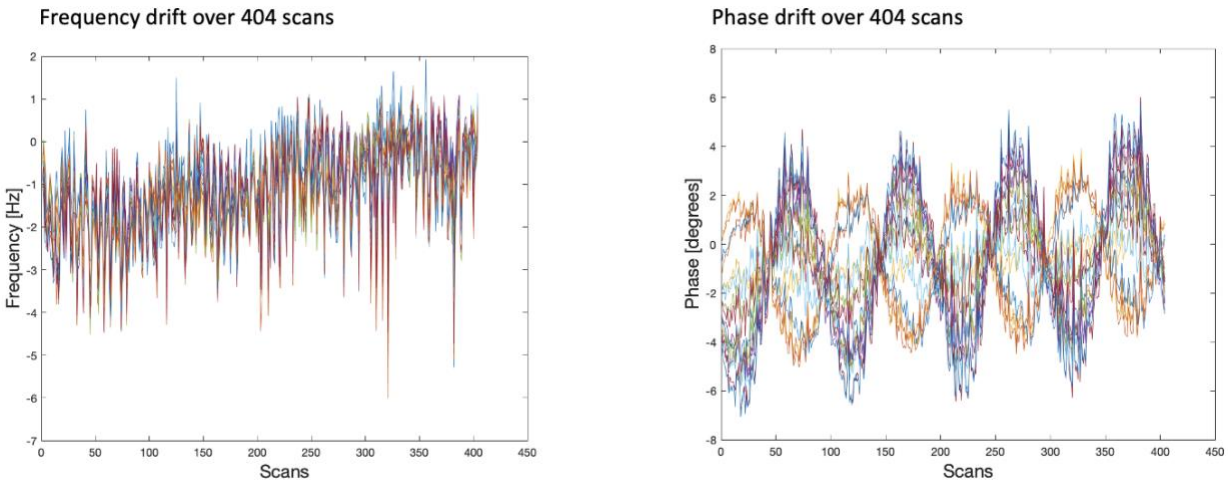

Figure 4-8: (A) Plot of frequency drift measured for each coil channel and shot over 404 scans (101 shots x 4 averages). The total drift was estimated to be 0.36Hz/min in the phantom, with a total drift of 3.6Hz. (B) The phase drift measured for each coil channel and shot over 404 scans. The estimated phase drift did not exceed ±6 degrees

Water suppressed spectra from an arbitrarily selected voxel of interest in the reconstructed MRSI grid are shown in Figure 4-9, both before and after drift correction. Frequency and phase drift correction resulted in a slight visual improvement in lineshapes of NAA, Cr, Cho and mI peaks. However, the improvement was more difficult to assess due to the presence of spectral artifacts, such as the large hump between 2-3 ppm. Future work is yet to be done to improve *in vivo* spectral quality in order to reliably estimate the improvement in spectra post-spectral registration.

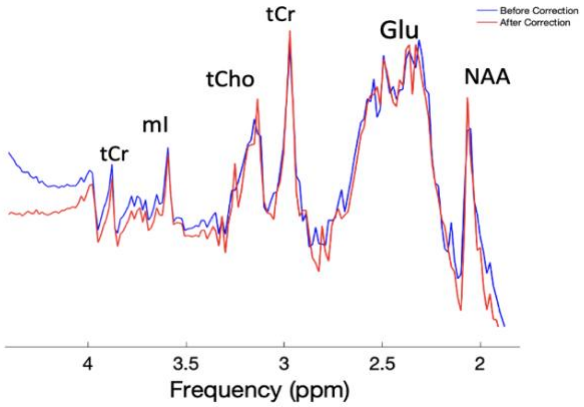

Figure 4-9: Corrected (red) and uncorrected (blue) MRS spectra from an arbitrarily chosen voxel from the in vivo Rosette-MRSI acquisition with N_x=64, after processing. Some improvement in lineshapes of NAA, tCho, tCr and mI is seen post drift correction, however the overall spectral quality is poor due to spectral artefacts.

4.3 Data Acquisition at 7T

Representative Rosette-MRSI phantom spectra from an arbitrarily selected voxel of interest, acquired at 3T and 7T are shown in Figure 4-10. As expected, the 7T spectrum appears to have sharper linewidth and improved SNR compared to 3T.

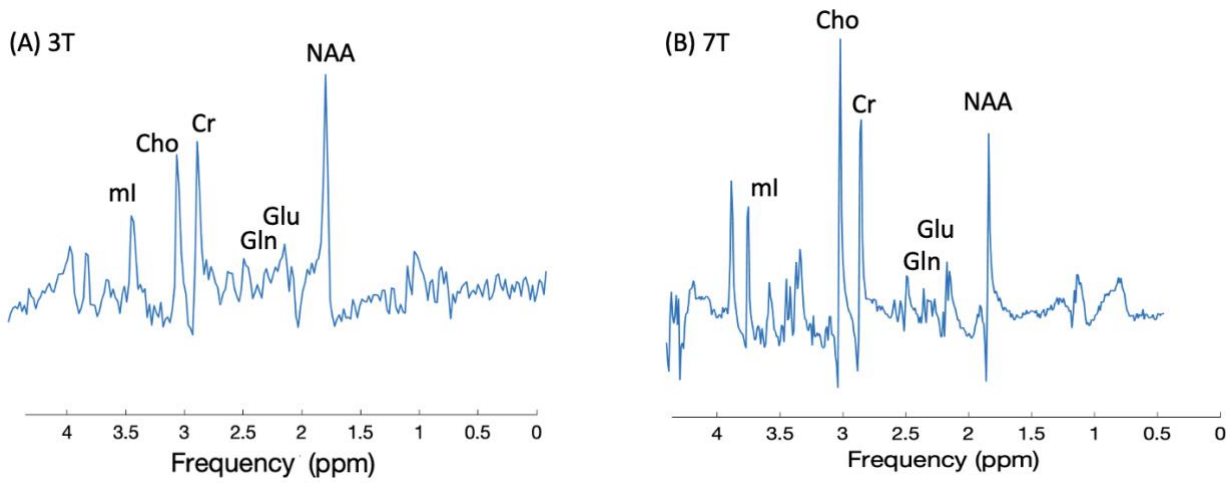

Figure 4-10: Representative phantom spectra at (A)3T and (B)7T from an arbitrarily selected voxel. Major metabolite peaks are labelled.

Figure 4-11 shows SNR and NAA linewidth maps for 3T and 7T phantom data. The mean value of SNR at 3T was calculated to be 155.09± 25.54 and the value at 7T was 162.89±31.40 ($p<0.001$).

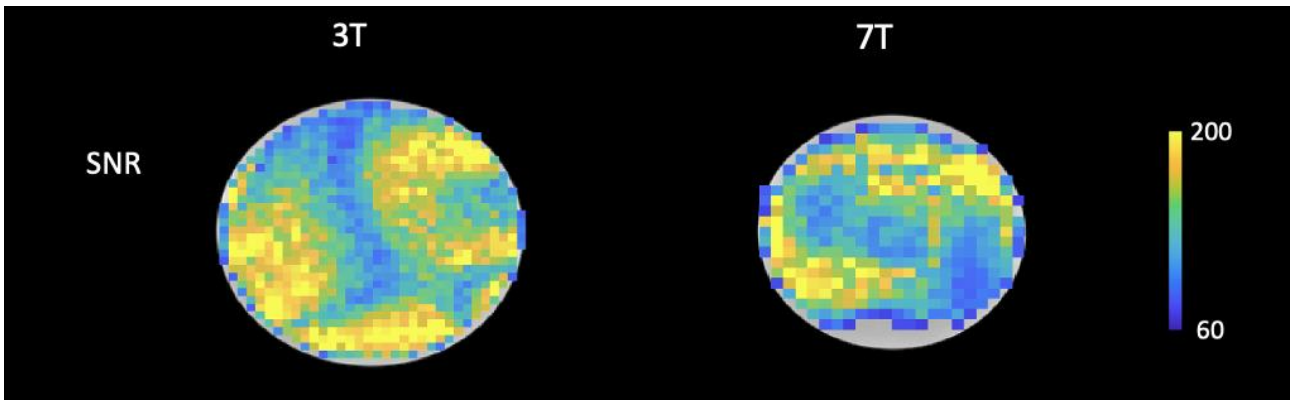

Figure 4-11: (A)SNR (measured as the amplitude of the NAA peak divided by the standard deviation of the noise) maps in 64x64 resolution (left) for 3T and 48x48 resolution for 7T phantom data showing signal pixel intensity distribution across the whole 2-D phantom slice.

Figure 4-12 shows LCModel fit results for phantom MRSI spectra acquired at 3T and 7T. Metabolite concentrations and CRLB value comparisons are given in Table 4-2.

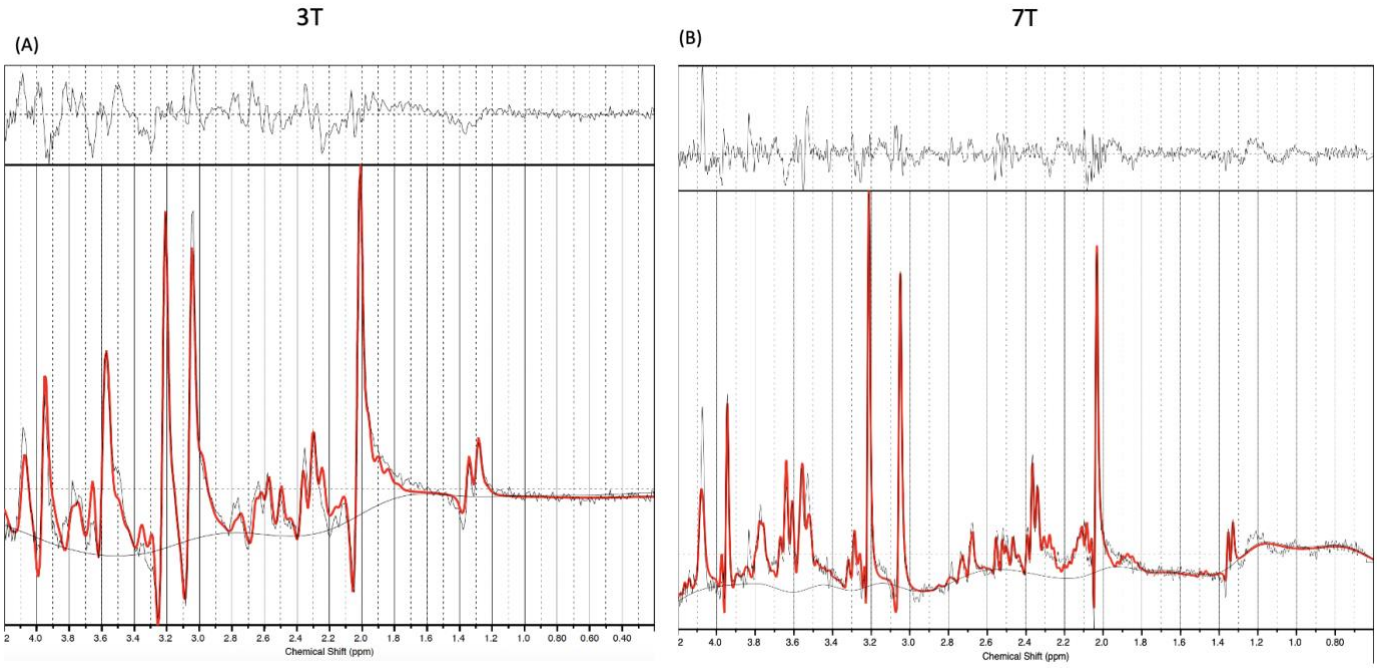

Figure 4-12: Results of LCModel fitting analysis for phantom MRSI spectra are shown. LCModel fit is shown by the red line. Representative spectrum is depicted by the black line and fit residual (difference between data and fit) is shown at the top (black line).

Table 4-2

Metabolite concentration ratios with respect to total creatine (tCr) and, CRLB values at 3T and 7T are given. Metabolite fittings with CRLB>20% were excluded from analysis and shown as NA (Not available). Measurement precision was improved at 7T.

	Metabolite concentration ratios with respect tCr at 3T	%CRLB at 3T	Metabolite concentration ratios with respect tCr at 7T	%CRLB at 7T
PCh	0.403	6	0.296	2
Cr	NA	NA	0.749	3
PCr	0.908	9	0.251	6
GABA	0.656	14	NA	NA
Gln	NA	NA	0.167	11
Glu	0.743	12	1.059	2
Gly	NA	NA	0.200	8
Ins	1.042	8	1.16	3
Lac	0.385	14	0.201	6
NAA	1.247	6	0.660	3
Glc	NA	NA	0.342	9
GPC	NA	NA	6.8E-02	7
Asc	NA	NA	0.652	5

Chapter 5: Discussion

5.1 Rapid high-resolution MRSI development

Time-efficient data acquisition in MRSI has been identified as one of the major limiting factors for high spatial resolution whole-brain metabolic mapping. Although a number of rapid high-resolution MRSI techniques have been proposed [135], they are not widely available and there is a great need for development in this area. We demonstrated the implementation of a Rosette-MRSI pulse sequence that yielded a high spatial resolution in a reasonable scan time. Rosette encoding provided about 40 times faster mapping than conventional phase encoded MRSI for the same spatial resolution. For example, if the same TR was used for both rosette and conventional MRSI (say 700ms), acquiring a single average of Rosette-MRSI with Nx=64 requires 101 shots, which would take 101 x 700 ms = 1 minute 17 seconds. By contrast, a single average conventional MRSI acquisition with the same spatial resolution would take 64x64x700ms = ~48min. Such a long scan duration for conventional MRSI is impractical in a clinical setting where short scan durations are required. It becomes even more impractical when considering that both water unsuppressed and water suppressed scans are typically needed in a single experiment, for processing and quantification. The rapid encoding of the rosette sequence conveniently allows the user to select the required number of averages for sufficient SNR in the water suppressed scan, while also maintaining a very short water unsuppressed scan (1 or 2 averages), since the water signal is strong and requires little or no averaging. Accelerated MRSI also makes dynamic experiments such as fMRS (functional MRS) and dynamic ^{13}C MRSI possible. The approach will allow simultaneous mapping of brain chemistry and metabolism and may be useful in characterizing disease progression and treatment response in neurological disorders. These advances point towards the vast clinical potential of whole brain fast spectroscopic imaging techniques.

5.1.1 Trajectory design

Based on scanner hardware constrains (sampling rate, gradient limits and slew rate limits) we designed optimal rosette trajectories that provided accelerated k-space coverage for a given spectral bandwidth and spatial resolution. Our results supported the first hypothesis of Rosette-MRSI being able to achieve high spatial resolutions in a short scan time (~10min). Given the rapid encoding time (a 64 x 64 matrix fully sampled in just over 1 minute), it may be possible to achieve even shorter scan durations, be we expect shorter scan durations to yield lower SNR which may compromise MRSI quantification accuracy. The achievable spectral bandwidth and/or spatial resolution at ultra-high field strengths was limited by slew rate limitations [166, 167]. Although sufficient spectral bandwidth was achieved at 7T with a nominal voxel size of 7 x 7 x 10 mm^3, going to higher spatial resolutions for the same bandwidth will require the use of temporal interleaves in the rosette trajectory. Temporal interleaves will be able to alleviate slew rate restrictions at the cost of acquisition time [13]. It has been shown that using two temporal interleaves in rosette trajectories, which is done by adding a second set of trajectories, time delayed with respect to the first one, doubles the spectral bandwidth [148].

Density compensation for the rosette k-space trajectory was performed using a simulated trajectory matching the acquisition parameters that idealized the scanner's physical environment. However, the actual k-space trajectory could very well be impeded by B_0 inhomogeneity effects, gradient heating due to eddy currents and other system imperfections [168]. These sampling inaccuracies can lead to off-resonance contributions leading to background noise and artifacts in the reconstructed data. Therefore, knowledge of MR system deviations is crucial to reliably reconstructing spectra from the acquired data. The gradient waveforms and k-space trajectories can be estimated using a dynamic field camera (Skope, Zurich, Switzerland) that will allow for accurate characterization of gradient systems [169]. Using this information to perform k-space density compensation can help in eliminating the existing spectral artifacts.

5.1.2 Assessing spectral quality

Results from phantom experiments at 3T and 7T yielded reliable and quantifiable results with good spectral quality. However, results from in-vivo experiments at both field strengths were contaminated by residual extracranial lipids especially upfield of the NAA resonance (between 1-2 ppm) and around the glutamate resonance (between 2-3 ppm). These artefacts are the result of "voxel bleeding" due to the imperfect point-spread function as shown in Figure 1-6 above. This sinc-shaped point-spread function causes each voxel to contain contamination from remote regions. Since lipids exist in very high concentrations in the extracranial space (in the scalp), even a small amount of voxel bleeding can cause noticeable lipid contamination throughout the brain.

The spectral artifacts believed to be caused by voxel bleeding can possibly be eliminated by the following recommendations:

(i) *Prospective lipid suppression*: Our current experimental protocol utilized L2 regularisation during post-processing to remove lipids in the acquired Rosette-MRSI spectra. In practice, L2 lipid regularisation is known to provide lipid reduction factors in the order of 10-fold [170, 171]. While this technique was successful in removing most of the lipid signal in the 0.3-1.8 ppm range and in improving the appearance of NAA peak, applying it in the other positions of interest (for example, 2.05 ppm, 2.24 ppm and 2.81 ppm) would have removed metabolites of interest. Therefore, implementing prospective lipid suppression using approaches like outer-volume suppression (OVS) [172, 173] or spectrally selective suppression might help removing lipid contamination more reliably without sacrificing the metabolite appearances in the spectra.

(ii) *Lipid crusher coil*: Boer et al. proposed the approach of using outer volume crusher coils to suppress extra cranial lipids [174]. This is based on the principle of surface spoiling gradients, which generate a local distortion in B_0 field in the cranial layer, thereby destroying the phase coherence of extra cranial lipid signals. This technique is capable of achieving lipid suppression factors in the order of 20-70-fold [170].

(iii) *Using a longer echo time*: Since lipid signals have a shorter T2 relaxation time than metabolites, using longer echo times (~130ms) might help reduce the appearance of lipid contamination in the MRS/MRSI spectra. This would have to be implemented in a spin-echo acquisition, since longer echo times would suffer from huge baseline distortions in pulse and acquire sequences.

(iv) *Improving B_0 shimming*: A completely homogenous B_0 field possesses the same amplitude throughout the region of interest. However, owing to system imperfections and variations in magnetic susceptibility of substances, the resulting B_0 field is inhomogeneous [175, 176]. The major source of magnetic field distortions *in-vivo* is the vast differences in magnetic susceptibilities between brain tissue and air from nasal and auditory passages [176]. These deviations can adversely affect the spectral quality and impede the application of post-processing methods that rely on the exact frequency definition. While we performed both whole brain and head shim, the results still required improvement in shimming.

Using an echo delay of 1.8ms induced first-order phase distortions that were noticeable in both phantom and human brain spectra. Although we attempted to remove this effect in post-processing by a first-order phase correction, some residual baseline distortion remained following correction. This effect can be further reduced by using an even shorter echo delay or eliminated completely by using a spin echo sequence to automatically remove first order phase errors. In addition to this, spatial non-uniformity was observed in the SNR and linewidth maps (Figure 4-11) most likely due to field inhomogeneity.

5.2 Frequency and phase drift correction

The application of spectral registration to the acquired Rosette-MRSI data was demonstrated in both phantom and *in-vivo* experiments to correct for frequency and phase drifts induced by heating of gradient coils and passive shimming that can unfavorably affect the acquired MRSI data. Spectral registration works by optimally aligning all FIDs acquired at a common k-space point (the origin in the case of rosette trajectories) to a reference spectrum (the first k=0 FID in the series) and applies these corrections to the entire k-space to retrospectively remove the effects of B0 drift. Our results confirm our 2nd hypothesis that spectral registration enables accurate estimation and correction of frequency and phase offsets, resulting in significantly improved MRSI spectral quality (reported in Table 4-1). These improvements in spectral quality are important for ensuring the accuracy of spectral quantification.

5.3 Comparison of results between 3T and 7T MRI scanner systems

7T MR systems offer a significant increase in SNR, which allows spectroscopic imaging with high spatial and spectral resolution. These improvements provide high anatomic detail and therefore higher diagnostic confidence [177]. However, these advantages come at the cost of a significantly greater RF power deposition (measured in terms of specific absorption rate (SAR)) and higher B_0 and B_1 inhomogeneity [178]. Inhomogeneous B_0 conditions reduce the water suppression efficiency resulting in a spread of water frequencies instead of a single frequency [176]. These suboptimal B_0 conditions may thus cause SNR gains at higher field strengths to fall below the theoretically attainable limit [179], unless appropriate localised shimming is achieved [180, 181]. Therefore, comparison of results between scanners operating at different field strengths is important for evaluating if the benefits at ultra-high fields outweigh the existing technical challenges.

The Rosette-MRSI sequence was implemented on both 3T and 7T MR systems, with the goal of being able to perform metabolite mapping in both clinical and cutting-edge research settings. The comparison of Rosette-MRSI results was performed between 3T and 7T scanner systems with an

intention to assess the precision with which metabolites can be quantified reliably at both field strengths, which would provide a basis for the clinical application of Rosette-MRSI for the optimal assessment of alterations in metabolic concentrations in disease. While sequence refinements are needed to reliably quantify data *in-vivo*, our phantom results confirmed our 3rd hypothesis. Measurement precision was improved at 7T as reflected by our LCModel quantification results. While the current study attempted to match the methodology at both field strengths, the SNR was comparable at 3T and 7T, contrary to an expected significant gain at 7T. This might have been because a lower spectral bandwidth could not be achieved for the same k-space trajectory design owing to minimum spectral resolution requirements to resolve metabolic resonances at higher field strengths.

Chapter 6: Conclusion

Here, we demonstrated the development and implementation of an FID-based ^{1}H Rosette-MRSI sequence in phantoms and *in-vivo*. The technique, in combination with advanced processing techniques, enabled reliable detection and quantification of important metabolites including tNAA, tCho, tCr, Lac, mI and Glx in phantoms. While future work needs to be done to eliminate spectral artifacts caused due to lipid contamination in the reconstructed *in-vivo* data, Rosette-MRSI has huge potential for clinical translation owing to its ability to yield high-quality spectra in reasonable scan times. We further demonstrated the feasibility of frequency and phase drift correction in rosette trajectories which can't be performed in other commonly used trajectories like EPSI, concentric rings and conventional MRSI without the use of separately acquired navigator echoes. We also showed that Rosette-MRSI acquisition allows fast, high-resolution MRSI to be acquired at both field strengths (3T and 7T) with reliable concentration measures. Thus, we believe that Rosette-MRSI offers substantial potential for clinical and experimental MRSI compared to other accelerated MR spectroscopic imaging techniques. Transparency and reproducibility are crucial features that allow science to improve and evolve continuously. To this end, we aim to share our developed Rosette-FID sequence with researchers worldwide in order for the technique to gain potential universal application.

References

1. Iqbal, Z., et al., *Super-Resolution (1)H Magnetic Resonance Spectroscopic Imaging Utilizing Deep Learning.* Front Oncol, 2019. **9**: p. 1010.
2. Govindaraju, V., K. Young, and A.A. Maudsley, *Proton NMR chemical shifts and coupling constants for brain metabolites.* NMR Biomed, 2000. **13**(3): p. 129-53.
3. Stagg, C. and D. Rothman, *Magnetic Resonance Spectroscopy: Tools for Neuroscience Research and Emerging Clinical Applications*. 2014. 1-376.
4. Watts, M.E., R. Pocock, and C. Claudianos, *Brain Energy and Oxygen Metabolism: Emerging Role in Normal Function and Disease.* Front Mol Neurosci, 2018. **11**: p. 216.
5. Berrington, A., *Magnetic resonance spectroscopy of the in vivo brain with semi-LASER*. 2017, University of Oxford.
6. Kantarci, K., *1H magnetic resonance spectroscopy in dementia.* Br J Radiol, 2007. **80 Spec No 2**: p. S146-52.
7. Martin, W.R., *MR spectroscopy in neurodegenerative disease.* Mol Imaging Biol, 2007. **9**(4): p. 196-203.
8. Wang, H., et al., *Magnetic Resonance Spectroscopy in Alzheimer's Disease: Systematic Review and Meta-Analysis.* J Alzheimers Dis, 2015. **46**(4): p. 1049-70.
9. Zhang, Y., et al., *Comparison of reproducibility of single voxel spectroscopy and whole-brain magnetic resonance spectroscopy imaging at 3T.* NMR Biomed, 2018. **31**(4): p. e3898.
10. Rosen, Y. and R.E. Lenkinski, *Recent advances in magnetic resonance neurospectroscopy.* Neurotherapeutics, 2007. **4**(3): p. 330-45.
11. Graaf, R.A.d., *In Vivo NMR Spectroscopy—2nd Edition: Principles and Techniques.* 2 ed. 2007, New York, NY: Wiley.
12. Bernstein, M.A., K.F. King, and X.J. Zhou, *Handbook of MRI Pulse Sequences*. 1 ed. 2004: Elsevier.
13. Bogner, W., R. Otazo, and A. Henning, *Accelerated MR spectroscopic imaging-a review of current and emerging techniques.* NMR Biomed, 2021. **34**(5): p. e4314.
14. Purcell, E.M., H.C. Torrey, and R.V. Pound, *Resonance Absorption by Nuclear Magnetic Moments in a Solid.* Physical Review, 1946. **69**(1-2): p. 37-38.
15. Bloch, F., *Nuclear Induction.* Physical Review, 1946. **70**(7-8): p. 460-474.
16. Hoult, D.I., et al., *Observation of tissue metabolites using 31P nuclear magnetic resonance.* Nature, 1974. **252**(5481): p. 285-7.
17. Ackerman, J.J., et al., *Mapping of metabolites in whole animals by 31P NMR using surface coils.* Nature, 1980. **283**(5743): p. 167-70.
18. Behar, K.L., et al., *High-resolution 1H nuclear magnetic resonance study of cerebral hypoxia in vivo.* Proc Natl Acad Sci U S A, 1983. **80**(16): p. 4945-8.
19. Longmore, D.B., *The principles of magnetic resonance.* Br Med Bull, 1989. **45**(4): p. 848-80.
20. Proctor, W.G. and F.C. Yu, *The Dependence of a Nuclear Magnetic Resonance Frequency upon Chemical Compound.* Physical Review, 1950. **77**(5): p. 717-717.
21. Simpson, R., et al., *Advanced processing and simulation of MRS data using the FID appliance (FID-A)-An open source, MATLAB-based toolkit.* Magn Reson Med, 2017. **77**(1): p. 23-33.
22. Zhou, Y. and N.C. Danbolt, *Glutamate as a neurotransmitter in the healthy brain.* J Neural Transm (Vienna), 2014. **121**(8): p. 799-817.
23. Citri, A. and R.C. Malenka, *Synaptic plasticity: multiple forms, functions, and mechanisms.* Neuropsychopharmacology, 2008. **33**(1): p. 18-41.
24. Deuchars, S. and J. Deuchars, *Neuroscience—a novelty for the nervous: Neuroscience (1997). Purves D, Augustine GJ, Fitzpatrick D, Katz LC, LaMantia A-S, McNamara JO (Eds). Sunderland, MA: Sinauer Associates, Inc. 562 pp.* BioEssays, 1998. **20**(10): p. 871-872.
25. Underhill, S. and S. Amara, *TRANSPORTERS | Glutamate Transporters in Epilepsy*, in *Encyclopedia of Basic Epilepsy Research*, P.A. Schwartzkroin, Editor. 2009, Academic Press: Oxford. p. 1398-1405.

26. Petroff, O.A.C., *6 - Metabolic Biopsy of the Brain*, in *Molecular Neurology*, S.G. Waxman, Editor. 2007, Academic Press: San Diego. p. 77-100.
27. Christoph Juchem and D.L. Rothman, *Basis of Magnetic Resonance. Magnetic Resonance Spectroscopy: Tools for Neuroscience Research and Emerging Clinical Applications*. 1 ed. 2013: Elsevier Inc.
28. Ramadan, S., A. Lin, and P. Stanwell, *Glutamate and glutamine: a review of in vivo MRS in the human brain.* NMR Biomed, 2013. **26**(12): p. 1630-46.
29. Hingerl, L., et al., *Clinical High-Resolution 3D-MR Spectroscopic Imaging of the Human Brain at 7 T.* Investigative Radiology, 2019. **55**: p. 1.
30. Dringen, R., *Metabolism and functions of glutathione in brain.* Prog Neurobiol, 2000. **62**(6): p. 649-71.
31. Lu, S.C., *Glutathione synthesis.* Biochimica et Biophysica Acta (BBA) - General Subjects, 2013. **1830**(5): p. 3143-3153.
32. McCormick, D.A., *GABA as an inhibitory neurotransmitter in human cerebral cortex.* J Neurophysiol, 1989. **62**(5): p. 1018-27.
33. Fitsanakis, V.A. and M. Aschner, *The importance of glutamate, glycine, and gamma-aminobutyric acid transport and regulation in manganese, mercury and lead neurotoxicity.* Toxicol Appl Pharmacol, 2005. **204**(3): p. 343-54.
34. Weis, J., et al., *GABA quantification in human anterior cingulate cortex.* PLoS One, 2021. **16**(1): p. e0240641.
35. Rothman, D.L., et al., *Localized 1H NMR measurements of gamma-aminobutyric acid in human brain in vivo.* Proc Natl Acad Sci U S A, 1993. **90**(12): p. 5662-6.
36. Mescher, M., et al., *Simultaneous in vivo spectral editing and water suppression.* NMR Biomed, 1998. **11**(6): p. 266-72.
37. Mullins, P.G., et al., *Current practice in the use of MEGA-PRESS spectroscopy for the detection of GABA.* NeuroImage, 2014. **86**: p. 43-52.
38. Oja, S.S. and P. Saransaari, *Taurine and epilepsy.* Epilepsy Res, 2013. **104**(3): p. 187-94.
39. Lombardini, J.B., *Taurine depletion in the intact animal stimulates in vitro phosphorylation of an approximately 44-kDa protein present in the mitochondrial fraction of the rat heart.* J Mol Cell Cardiol, 1996. **28**(9): p. 1957-61.
40. El Idrissi, A. and W.J. L'Amoreaux, *Selective resistance of taurine-fed mice to isoniazide-potentiated seizures: in vivo functional test for the activity of glutamic acid decarboxylase.* Neuroscience, 2008. **156**(3): p. 693-9.
41. Kumari, N., H. Prentice, and J.Y. Wu, *Taurine and its neuroprotective role.* Adv Exp Med Biol, 2013. **775**: p. 19-27.
42. Schaffer, S.W., V. Solodushko, and D. Kakhniashvili, *Beneficial effect of taurine depletion on osmotic sodium and calcium loading during chemical hypoxia.* Am J Physiol Cell Physiol, 2002. **282**(5): p. C1113-20.
43. Haris, M., et al., *In vivo mapping of brain myo-inositol.* Neuroimage, 2011. **54**(3): p. 2079-85.
44. Brand, A., C. Richter-Landsberg, and D. Leibfritz, *Multinuclear NMR studies on the energy metabolism of glial and neuronal cells.* Dev Neurosci, 1993. **15**(3-5): p. 289-98.
45. Saiardi, A., et al., *Phosphorylation of proteins by inositol pyrophosphates.* Science, 2004. **306**(5704): p. 2101-5.
46. Chhetri, D.R., *Myo-Inositol and Its Derivatives: Their Emerging Role in the Treatment of Human Diseases.* Front Pharmacol, 2019. **10**: p. 1172.
47. York, J.D., et al., *A phospholipase C-dependent inositol polyphosphate kinase pathway required for efficient messenger RNA export.* Science, 1999. **285**(5424): p. 96-100.
48. Zeisel, S.H. and J.K. Blusztajn, *Choline and human nutrition.* Annu Rev Nutr, 1994. **14**: p. 269-96.
49. Zeisel, S.H., *Choline: Needed for Normal Development of Memory.* Journal of the American College of Nutrition, 2000. **19**(sup5): p. 528S-531S.
50. Haddadin, I.S., et al., *Metabolite quantification and high-field MRS in breast cancer.* NMR Biomed, 2009. **22**(1): p. 65-76.
51. Prvulovic Bunovic, N., et al., *Is Elevated Choline on Magnetic Resonance Spectroscopy a Reliable Marker of Breast Lesion Malignancy?* Front Oncol, 2021. **11**: p. 610354.

52. Nelson, S.J., *Multivoxel magnetic resonance spectroscopy of brain tumors.* Mol Cancer Ther, 2003. **2**(5): p. 497-507.
53. Hauser, T., et al., *[MR spectroscopy in dementia].* Radiologe, 2010. **50**(9): p. 791-8.
54. Llufriu, S., et al., *Magnetic Resonance Spectroscopy Markers of Disease Progression in Multiple Sclerosis.* JAMA Neurology, 2014. **71**(7): p. 840-847.
55. Marjańska, M., et al., *Region-specific aging of the human brain as evidenced by neurochemical profiles measured noninvasively in the posterior cingulate cortex and the occipital lobe using (1)H magnetic resonance spectroscopy at 7 T.* Neuroscience, 2017. **354**: p. 168-177.
56. Wyss, M. and R. Kaddurah-Daouk, *Creatine and creatinine metabolism.* Physiol Rev, 2000. **80**(3): p. 1107-213.
57. Ingwall, J.S., et al., *The creatine kinase system in normal and diseased human myocardium.* N Engl J Med, 1985. **313**(17): p. 1050-4.
58. Neubauer, S., et al., *Downregulation of the Na(+)-creatine cotransporter in failing human myocardium and in experimental heart failure.* Circulation, 1999. **100**(18): p. 1847-50.
59. Hui, S., et al., *Glucose feeds the TCA cycle via circulating lactate.* Nature, 2017. **551**(7678): p. 115-118.
60. Rudkin, T.M. and D.L. Arnold, *Proton Magnetic Resonance Spectroscopy for the Diagnosis and Management of Cerebral Disorders.* Archives of Neurology, 1999. **56**(8): p. 919-926.
61. Ford, T.C. and D.P. Crewther, *A Comprehensive Review of the 1H-MRS Metabolite Spectrum in Autism Spectrum Disorder.* Frontiers in Molecular Neuroscience, 2016. **9**.
62. Moffett, J.R., et al., *N-Acetylaspartate in the CNS: from neurodiagnostics to neurobiology.* Prog Neurobiol, 2007. **81**(2): p. 89-131.
63. Chugani, D.C., et al., *Evidence of altered energy metabolism in autistic children.* Prog Neuropsychopharmacol Biol Psychiatry, 1999. **23**(4): p. 635-41.
64. Taylor, D.L., et al., *Investigation into the role of N-acetylaspartate in cerebral osmoregulation.* J Neurochem, 1995. **65**(1): p. 275-81.
65. Wittsack, H.J., et al., *Quantitative measurements with localized 1H MR spectroscopy in children with Canavan's disease.* J Magn Reson Imaging, 1996. **6**(6): p. 889-93.
66. Chiappelli, J., et al., *Cardiovascular risks impact human brain N-acetylaspartate in regionally specific patterns.* Proceedings of the National Academy of Sciences, 2019. **116**(50): p. 25243-25249.
67. Tsai, G. and J.T. Coyle, *N-acetylaspartate in neuropsychiatric disorders.* Prog Neurobiol, 1995. **46**(5): p. 531-40.
68. Behar, K.L. and T. Ogino, *Characterization of macromolecule resonances in the 1H NMR spectrum of rat brain.* Magn Reson Med, 1993. **30**(1): p. 38-44.
69. Kauppinen, R.A., et al., *Quantitative analysis of 1H NMR detected proteins in the rat cerebral cortex in vivo and in vitro.* NMR Biomed, 1993. **6**(4): p. 242-7.
70. Cudalbu, C., et al., *Contribution of macromolecules to brain (1) H MR spectra: Experts' consensus recommendations.* NMR Biomed, 2021. **34**(5): p. e4393.
71. Behar, K.L., et al., *Analysis of macromolecule resonances in 1H NMR spectra of human brain.* Magn Reson Med, 1994. **32**(3): p. 294-302.
72. Gordon, B.A., et al., *Spatial patterns of neuroimaging biomarker change in individuals from families with autosomal dominant Alzheimer's disease: a longitudinal study.* Lancet Neurol, 2018. **17**(3): p. 241-250.
73. Maul, S., I. Giegling, and D. Rujescu, *Proton Magnetic Resonance Spectroscopy in Common Dementias—Current Status and Perspectives.* Frontiers in Psychiatry, 2020. **11**.
74. Klietz, M., et al., *Altered Neurometabolic Profile in Early Parkinson's Disease: A Study With Short Echo-Time Whole Brain MR Spectroscopic Imaging.* Frontiers in Neurology, 2019. **10**.
75. Pini, L., et al., *Brain atrophy in Alzheimer's Disease and aging.* Ageing Res Rev, 2016. **30**: p. 25-48.
76. Markesbery, W.R., *Oxidative Stress Hypothesis in Alzheimer's Disease.* Free Radical Biology and Medicine, 1997. **23**(1): p. 134-147.
77. De Felice, F.G., M.V. Lourenco, and S.T. Ferreira, *How does brain insulin resistance develop in Alzheimer's disease?* Alzheimer's & Dementia, 2014. **10**(1, Supplement): p. S26-S32.

78. Chen, Z. and C. Zhong, *Decoding Alzheimer's disease from perturbed cerebral glucose metabolism: Implications for diagnostic and therapeutic strategies.* Progress in Neurobiology, 2013. **108**: p. 21-43.
79. Phelps, M.E., et al., *Tomographic measurement of local cerebral glucose metabolic rate in humans with (F-18)2-fluoro-2-deoxy-D-glucose: validation of method.* Ann Neurol, 1979. **6**(5): p. 371-88.
80. Silverman, D.H., et al., *Evaluating early dementia with and without assessment of regional cerebral metabolism by PET: a comparison of predicted costs and benefits.* J Nucl Med, 2002. **43**(2): p. 253-66.
81. Morbelli, S., et al., *A Cochrane review on brain [¹⁸F]FDG PET in dementia: limitations and future perspectives.* Eur J Nucl Med Mol Imaging, 2015. **42**(10): p. 1487-91.
82. Lim, H.S., et al., *FDG PET/CT for the detection and evaluation of breast diseases: usefulness and limitations.* Radiographics, 2007. **27 Suppl 1**: p. S197-213.
83. Kwon, H.W., et al., *Radiation Dose from Whole-Body F-18 Fluorodeoxyglucose Positron Emission Tomography/Computed Tomography: Nationwide Survey in Korea.* J Korean Med Sci, 2016. **31 Suppl 1**(Suppl 1): p. S69-74.
84. Fayed, N., et al., *Brain glutamate levels are decreased in Alzheimer's disease: a magnetic resonance spectroscopy study.* Am J Alzheimers Dis Other Demen, 2011. **26**(6): p. 450-6.
85. Huang, W., et al., *High brain myo-inositol levels in the predementia phase of Alzheimer's disease in adults with Down's syndrome: a 1H MRS study.* Am J Psychiatry, 1999. **156**(12): p. 1879-86.
86. Modrego, P.J., et al., *Changes in metabolite ratios after treatment with rivastigmine in Alzheimer's disease: a nonrandomised controlled trial with magnetic resonance spectroscopy.* CNS Drugs, 2006. **20**(10): p. 867-77.
87. Zaccagna, F., et al., *Hyperpolarized carbon-13 magnetic resonance spectroscopic imaging: a clinical tool for studying tumour metabolism.* Br J Radiol, 2018. **91**(1085): p. 20170688.
88. Beckmann, N., et al., *13C NMR for the assessment of human brain glucose metabolism in vivo.* Biochemistry, 1991. **30**(26): p. 6362-6.
89. van de Weijer, T. and V.B. Schrauwen-Hinderling, *Application of Magnetic Resonance Spectroscopy in metabolic research.* Biochimica et Biophysica Acta (BBA) - Molecular Basis of Disease, 2019. **1865**(4): p. 741-748.
90. Fox, N.C. and M.N. Rossor, *Seeing what Alzheimer saw--with magnetic resonance microscopy.* Nat Med, 2000. **6**(1): p. 20-1.
91. Drui, G., et al., *Loss of dopaminergic nigrostriatal neurons accounts for the motivational and affective deficits in Parkinson's disease.* Molecular Psychiatry, 2014. **19**(3): p. 358-367.
92. Hirsch, E.C., P. Jenner, and S. Przedborski, *Pathogenesis of Parkinson's disease.* Mov Disord, 2013. **28**(1): p. 24-30.
93. Giguère, N., S. Burke Nanni, and L.E. Trudeau, *On Cell Loss and Selective Vulnerability of Neuronal Populations in Parkinson's Disease.* Front Neurol, 2018. **9**: p. 455.
94. Abou-Sleiman, P.M., M.M. Muqit, and N.W. Wood, *Expanding insights of mitochondrial dysfunction in Parkinson's disease.* Nat Rev Neurosci, 2006. **7**(3): p. 207-19.
95. Hirsch, E.C., S. Vyas, and S. Hunot, *Neuroinflammation in Parkinson's disease.* Parkinsonism & Related Disorders, 2012. **18**: p. S210-S212.
96. Clarke, C.E. and M. Lowry, *Basal ganglia metabolite concentrations in idiopathic Parkinson's disease and multiple system atrophy measured by proton magnetic resonance spectroscopy.* Eur J Neurol, 2000. **7**(6): p. 661-5.
97. Oz, G., et al., *Proton MRS of the unilateral substantia nigra in the human brain at 4 tesla: detection of high GABA concentrations.* Magn Reson Med, 2006. **55**(2): p. 296-301.
98. Ciurleo, R., et al., *Magnetic Resonance Spectroscopy: An In Vivo Molecular Imaging Biomarker for Parkinson's Disease?* BioMed Research International, 2014. **2014**: p. 519816.
99. Masrori, P. and P. Van Damme, *Amyotrophic lateral sclerosis: a clinical review.* Eur J Neurol, 2020. **27**(10): p. 1918-1929.
100. Zarei, S., et al., *A comprehensive review of amyotrophic lateral sclerosis.* Surg Neurol Int, 2015. **6**: p. 171.
101. Kalra, S., *Magnetic Resonance Spectroscopy in ALS.* Frontiers in Neurology, 2019. **10**.

102. Cheong, I., et al., *Ultra-High Field Proton MR Spectroscopy in Early-Stage Amyotrophic Lateral Sclerosis.* Neurochem Res, 2017. **42**(6): p. 1833-1844.
103. Bruhn, H., et al., *Noninvasive differentiation of tumors with use of localized H-1 MR spectroscopy in vivo: initial experience in patients with cerebral tumors.* Radiology, 1989. **172**(2): p. 541-8.
104. Gupta, R.K., et al., *Relationships between choline magnetic resonance spectroscopy, apparent diffusion coefficient and quantitative histopathology in human glioma.* J Neurooncol, 2000. **50**(3): p. 215-26.
105. Horská, A. and P.B. Barker, *Imaging of brain tumors: MR spectroscopy and metabolic imaging.* Neuroimaging Clin N Am, 2010. **20**(3): p. 293-310.
106. Barker, P.B., J.D. Glickson, and R.N. Bryan, *In vivo magnetic resonance spectroscopy of human brain tumors.* Top Magn Reson Imaging, 1993. **5**(1): p. 32-45.
107. Herholz, K., et al., *In vivo imaging of glucose consumption and lactate concentration in human gliomas.* Ann Neurol, 1992. **31**(3): p. 319-27.
108. Alger, J.R., et al., *Metabolism of human gliomas: assessment with H-1 MR spectroscopy and F-18 fluorodeoxyglucose PET.* Radiology, 1990. **177**(3): p. 633-41.
109. Castillo, M., J.K. Smith, and L. Kwock, *Correlation of myo-inositol levels and grading of cerebral astrocytomas.* AJNR Am J Neuroradiol, 2000. **21**(9): p. 1645-9.
110. Howe, F.A., et al., *Metabolic profiles of human brain tumors using quantitative in vivo 1H magnetic resonance spectroscopy.* Magn Reson Med, 2003. **49**(2): p. 223-32.
111. Di Costanzo, A., et al., *Proton MR spectroscopy of cerebral gliomas at 3 T: spatial heterogeneity, and tumour grade and extent.* Eur Radiol, 2008. **18**(8): p. 1727-35.
112. Kuesel, A.C., et al., *1H MRS of high grade astrocytomas: mobile lipid accumulation in necrotic tissue.* NMR Biomed, 1994. **7**(3): p. 149-55.
113. Ghasemi, N., S. Razavi, and E. Nikzad, *Multiple Sclerosis: Pathogenesis, Symptoms, Diagnoses and Cell-Based Therapy.* Cell J, 2017. **19**(1): p. 1-10.
114. Kapeller, P., et al., *Quantitative 1H MRS imaging 14 years after presenting with a clinically isolated syndrome suggestive of multiple sclerosis.* Mult Scler, 2002. **8**(3): p. 207-10.
115. Vrenken, H., et al., *MR spectroscopic evidence for glial increase but not for neuro-axonal damage in MS normal-appearing white matter.* Magn Reson Med, 2005. **53**(2): p. 256-66.
116. Swanberg, K.M., et al., *Quantifying the Metabolic Signature of Multiple Sclerosis by in vivo Proton Magnetic Resonance Spectroscopy: Current Challenges and Future Outlook in the Translation From Proton Signal to Diagnostic Biomarker.* Frontiers in Neurology, 2019. **10**.
117. Nantes, J.C., et al., *GABA and glutamate levels correlate with MTR and clinical disability: Insights from multiple sclerosis.* Neuroimage, 2017. **157**: p. 705-715.
118. Muhlert, N., et al., *Memory in multiple sclerosis is linked to glutamate concentration in grey matter regions.* J Neurol Neurosurg Psychiatry, 2014. **85**(8): p. 833-9.
119. Srinivasan, R., et al., *Evidence of elevated glutamate in multiple sclerosis using magnetic resonance spectroscopy at 3 T.* Brain, 2005. **128**(Pt 5): p. 1016-25.
120. Azevedo, C.J., et al., *In vivo evidence of glutamate toxicity in multiple sclerosis.* Ann Neurol, 2014. **76**(2): p. 269-78.
121. Davie, C.A., et al., *Serial proton magnetic resonance spectroscopy in acute multiple sclerosis lesions.* Brain, 1994. **117 (Pt 1)**: p. 49-58.
122. Zaaraoui, W., et al., *Unfolding the long-term pathophysiological processes following an acute inflammatory demyelinating lesion of multiple sclerosis.* Magn Reson Imaging, 2010. **28**(4): p. 477-86.
123. Kocevar, G., et al., *Weekly follow up of acute lesions in three early multiple sclerosis patients using MR spectroscopy and diffusion.* J Neuroradiol, 2018. **45**(2): p. 108-113.
124. Choi, I.Y., et al., *Longitudinal changes of cerebral glutathione (GSH) levels associated with the clinical course of disease progression in patients with secondary progressive multiple sclerosis.* Mult Scler, 2017. **23**(7): p. 956-962.
125. van der Graaf, M., *In vivo magnetic resonance spectroscopy: basic methodology and clinical applications.* Eur Biophys J, 2010. **39**(4): p. 527-40.
126. Bertholdo, D., A. Watcharakorn, and M. Castillo, *Brain proton magnetic resonance spectroscopy: introduction and overview.* Neuroimaging Clin N Am, 2013. **23**(3): p. 359-80.
127. Frahm, J., et al., *Localized high-resolution proton NMR spectroscopy using stimulated echoes: initial applications to human brain in vivo.* Magn Reson Med, 1989. **9**(1): p. 79-93.

128. Al-Iedani, O., et al., *Fast magnetic resonance spectroscopic imaging techniques in human brain- applications in multiple sclerosis.* J Biomed Sci, 2017. **24**(1): p. 17.
129. Bottomley, P.A., *Spatial localization in NMR spectroscopy in vivo.* Ann N Y Acad Sci, 1987. **508**: p. 333-48.
130. Tkác, I., et al., *In vivo 1H NMR spectroscopy of rat brain at 1 ms echo time.* Magn Reson Med, 1999. **41**(4): p. 649-56.
131. Currie, S., et al., *Magnetic resonance spectroscopy of the brain.* Postgrad Med J, 2013. **89**(1048): p. 94-106.
132. Duijn, J.H., et al., *3D phase encoding 1H spectroscopic imaging of human brain.* Magn Reson Imaging, 1992. **10**(2): p. 315-9.
133. Li, Y., et al., *Considerations in applying 3D PRESS H-1 brain MRSI with an eight-channel phased-array coil at 3 T.* Magn Reson Imaging, 2006. **24**(10): p. 1295-302.
134. Ozhinsky, E., D.B. Vigneron, and S.J. Nelson, *Improved spatial coverage for brain 3D PRESS MRSI by automatic placement of outer-volume suppression saturation bands.* J Magn Reson Imaging, 2011. **33**(4): p. 792-802.
135. Pohmann, R., M. von Kienlin, and A. Haase, *Theoretical evaluation and comparison of fast chemical shift imaging methods.* J Magn Reson, 1997. **129**(2): p. 145-60.
136. Zierhut, M.L., et al., *(1)H spectroscopic imaging of human brain at 3 Tesla: comparison of fast three-dimensional magnetic resonance spectroscopic imaging techniques.* J Magn Reson Imaging, 2009. **30**(3): p. 473-80.
137. Serrai, H. and L. Senhadji, *Acquisition time reduction in magnetic resonance spectroscopic imaging using discrete wavelet encoding.* J Magn Reson, 2005. **177**(1): p. 22-30.
138. Mansfield, P., *Spatial mapping of the chemical shift in NMR.* Magn Reson Med, 1984. **1**(3): p. 370-86.
139. Adalsteinsson, E., et al., *Volumetric spectroscopic imaging with spiral-based k-space trajectories.* Magn Reson Med, 1998. **39**(6): p. 889-98.
140. Furuyama, J.K., N.E. Wilson, and M.A. Thomas, *Spectroscopic imaging using concentrically circular echo-planar trajectories in vivo.* Magn Reson Med, 2012. **67**(6): p. 1515-22.
141. Ramirez, M.S., et al., *Radial spectroscopic MRI of hyperpolarized [1-(13) C] pyruvate at 7 tesla.* Magn Reson Med, 2014. **72**(4): p. 986-95.
142. Pipe, J.G., *Motion correction with PROPELLER MRI: application to head motion and free-breathing cardiac imaging.* Magn Reson Med, 1999. **42**(5): p. 963-9.
143. Noll, D.C., *Multishot rosette trajectories for spectrally selective MR imaging.* IEEE Trans Med Imaging, 1997. **16**(4): p. 372-7.
144. Scheffler, K. and J. Hennig, *Frequency resolved single-shot MR imaging using stochastic k-space trajectories.* Magn Reson Med, 1996. **35**(4): p. 569-76.
145. Likes, R.S., *Moving gradient zeugmatography*. 1981: United States. p. Medium: X; Size: Pages: v 2008-02-07.
146. Noll, D.C., et al., *A homogeneity correction method for magnetic resonance imaging with time-varying gradients.* IEEE Trans Med Imaging, 1991. **10**(4): p. 629-37.
147. Schirda, C.V., C. Tanase, and F.E. Boada, *Rosette spectroscopic imaging: optimal parameters for alias-free, high sensitivity spectroscopic imaging.* J Magn Reson Imaging, 2009. **29**(6): p. 1375-85.
148. Schirda, C.V., *Rosette Spectroscopic Imaging* 2007, University of Pittsburgh. p. 148.
149. Robson, M.D., J.C. Gore, and R.T. Constable, *Measurement of the point spread function in MRI using constant time imaging.* Magn Reson Med, 1997. **38**(5): p. 733-40.
150. Helms, G. and A. Piringer, *Restoration of motion-related signal loss and line-shape deterioration of proton MR spectra using the residual water as intrinsic reference.* Magn Reson Med, 2001. **46**(2): p. 395-400.
151. Waddell, K.W., et al., *A practical guide to robust detection of GABA in human brain by J-difference spectroscopy at 3 T using a standard volume coil.* Magn Reson Imaging, 2007. **25**(7): p. 1032-8.
152. Dreher, W. and D. Leibfritz, *New method for the simultaneous detection of metabolites and water in localized in vivo 1H nuclear magnetic resonance spectroscopy.* Magn Reson Med, 2005. **54**(1): p. 190-5.

153. Near, J., et al., *Preprocessing, analysis and quantification in single-voxel magnetic resonance spectroscopy: experts' consensus recommendations.* NMR in Biomedicine, 2021. **34**(5): p. e4257.
154. Hock, A., et al., *Non-water-suppressed proton MR spectroscopy improves spectral quality in the human spinal cord.* Magn Reson Med, 2013. **69**(5): p. 1253-60.
155. Emir, U.E., et al., *Non-water-suppressed short-echo-time magnetic resonance spectroscopic imaging using a concentric ring k-space trajectory.* NMR Biomed, 2017. **30**(7).
156. Near, J., et al., *Frequency and phase drift correction of magnetic resonance spectroscopy data by spectral registration in the time domain.* Magn Reson Med, 2015. **73**(1): p. 44-50.
157. Peters, D.C., J.A. Derbyshire, and E.R. McVeigh, *Centering the projection reconstruction trajectory: reducing gradient delay errors.* Magn Reson Med, 2003. **50**(1): p. 1-6.
158. Rangwala, N., *Reduction of Artifacts Arising From Non-Ideal Gradients in Fast Magnetic Resonance Imaging*, in *Bioengineering*. 2011, University of Illinois at Chicago: Chicago, Illinois. p. 183.
159. Ogg, R.J., P.B. Kingsley, and J.S. Taylor, *WET, a T1- and B1-insensitive water-suppression method for in vivo localized 1H NMR spectroscopy.* J Magn Reson B, 1994. **104**(1): p. 1-10.
160. Marques, J.P., et al., *MP2RAGE, a self bias-field corrected sequence for improved segmentation and T1-mapping at high field.* Neuroimage, 2010. **49**(2): p. 1271-81.
161. Malik, W.Q., et al. *A gridding algorithm for efficient density compensation of arbitrarily sampled Fourier-domain data*. in *IEEE/Sarnoff Symposium on Advances in Wired and Wireless Communication.* 2005.
162. Bagchi, S. and S.K. Mitra, *The nonuniform discrete Fourier transform and its applications in filter design. I. 1-D.* IEEE Transactions on Circuits and Systems II: Analog and Digital Signal Processing, 1996. **43**(6): p. 422-433.
163. Vareth, M., et al., *A comparison of coil combination strategies in 3D multi-channel MRSI reconstruction for patients with brain tumors.* NMR Biomed, 2018. **31**(11): p. e3929.
164. Lin, L., et al., *Water removal in MR spectroscopic imaging with L2 regularization.* Magn Reson Med, 2019. **82**(4): p. 1278-1287.
165. Bilgic, B., et al., *Fast image reconstruction with L2-regularization.* J Magn Reson Imaging, 2014. **40**(1): p. 181-91.
166. Otazo, R., et al., *Signal-to-noise ratio and spectral linewidth improvements between 1.5 and 7 Tesla in proton echo-planar spectroscopic imaging.* Magn Reson Med, 2006. **56**(6): p. 1200-10.
167. Ebel, A., et al., *Achieving sufficient spectral bandwidth for volumetric 1H echo-planar spectroscopic imaging at 4 Tesla.* Magn Reson Med, 2005. **54**(3): p. 697-701.
168. Fischer, R.F., et al., *Monitoring and compensating phase imperfections in cine balanced steady-state free precession.* Magn Reson Med, 2013. **70**(6): p. 1567-79.
169. Vannesjo, S.J., et al., *Field camera measurements of gradient and shim impulse responses using frequency sweeps.* Magnetic Resonance in Medicine, 2014. **72**(2): p. 570-583.
170. Tkáč, I., et al., *Water and lipid suppression techniques for advanced (1) H MRS and MRSI of the human brain: Experts' consensus recommendations.* NMR Biomed, 2021. **34**(5): p. e4459.
171. Hangel, G., et al., *Ultra-high resolution brain metabolite mapping at 7 T by short-TR Hadamard-encoded FID-MRSI.* Neuroimage, 2018. **168**: p. 199-210.
172. Posse, S., et al., *MR spectroscopic imaging: principles and recent advances.* J Magn Reson Imaging, 2013. **37**(6): p. 1301-25.
173. Chu, A., et al., *Proton echo-planar spectroscopic imaging with highly effective outer volume suppression using combined presaturation and spatially selective echo dephasing.* Magn Reson Med, 2003. **49**(5): p. 817-21.
174. Boer, V.O., et al., *Lipid suppression for brain MRI and MRSI by means of a dedicated crusher coil.* Magnetic Resonance in Medicine, 2015. **73**(6): p. 2062-2068.
175. Schenck, J.F., *The role of magnetic susceptibility in magnetic resonance imaging: MRI magnetic compatibility of the first and second kinds.* Med Phys, 1996. **23**(6): p. 815-50.
176. Juchem, C. and R.A. de Graaf, *B(0) magnetic field homogeneity and shimming for in vivo magnetic resonance spectroscopy.* Anal Biochem, 2017. **529**: p. 17-29.

177. Aringhieri, G., V. Zampa, and M. Tosetti, *Musculoskeletal MRI at 7 T: do we need more or is it more than enough?* European Radiology Experimental, 2020. **4**(1): p. 48.
178. Deelchand, D.K., et al., *In vivo 1H NMR spectroscopy of the human brain at 9.4 T: initial results.* J Magn Reson, 2010. **206**(1): p. 74-80.
179. Barker, P.B., D.O. Hearshen, and M.D. Boska, *Single-voxel proton MRS of the human brain at 1.5T and 3.0T.* Magn Reson Med, 2001. **45**(5): p. 765-9.
180. Mekle, R., et al., *MR spectroscopy of the human brain with enhanced signal intensity at ultrashort echo times on a clinical platform at 3T and 7T.* Magn Reson Med, 2009. **61**(6): p. 1279-85.
181. Gruetter, R., et al., *Resolution improvements in in vivo 1H NMR spectra with increased magnetic field strength.* J Magn Reson, 1998. **135**(1): p. 260-4.